

Comparing 1-year GUMICS–4 simulations of the Terrestrial Magnetosphere with Cluster Measurements

G. Facskó^{1,2,3}, D. G. Sibeck², I. Honkonen⁴, L. Degener^{4*}, P. Peitso^{5†},
E. I. Tanskanen⁵, C. R. Anekallu⁶, J. Kalmár⁷, J. Bór⁷, G. Farinas Perez^{2,3‡},
S. Szalai^{7,8}, Á. Kis⁷, V. Wesztergom⁷

¹Wigner Research Centre for Physics, Budapest, Hungary

²NASA Goddard Space Flight Center, Greenbelt, Maryland, USA

³the Catholic University of America, Washington DC, USA

⁴Finnish Meteorological Institute, Helsinki, Finland

⁵Aalto University, School of Electrical Engineering, Espoo, Finland

⁶UCL Department of Space & Climate Physics, Mullard Space Science Laboratory, Dorking, UK

⁷Research Centre for Astronomy and Earth Sciences, Sopron, Hungary

⁸University of Miskolc, Department of Geophysics, Miskolc, Hungary

Key Points:

- The GUMICS–4 provides realistic ion plasma moments and magnetic field in the solar wind and the outer magnetosheath.
- The code can predict the realistic location of the bow shock.
- An inner magnetosphere model should be added to the code to increase the accuracy of the simulation.

*Now private individual, Hannover, Germany

†Now at Aurora Propulsion Technologies, Espoo, Finland

‡Now at University of Miami, Electrical and Computer Engineering Department, Miami, Florida, USA

Corresponding author: Gábor Facskó, gabor.i.facsko@gmail.com

20 **Abstract**

21 Previously a 1-year global magnetohydrodynamics simulation was made using the GUMICS–4
 22 code and the OMNI 1-min resolution solar wind data from January 29, 2002 to Febru-
 23 ary 2, 2003 as input. **From the saved simulation results parameters were dumpped**
 24 along the orbit of the Cluster SC3 reference spacecraft **to create a special product**
 25 **for further studies and validations.** We compare the saved parameters with the Clus-
 26 ter SC3 measurements. We use the magnetic field Z component, the solar wind veloc-
 27 ity X component and the solar wind density of the Cluster magnetometer, ion plasma
 28 and spacecraft potential measurements **in the** geocentric solar ecliptic reference frame,
 29 **respectively.** We select intervals in the solar wind, the magnetosheath and the mag-
 30 netosphere where the instruments above provided good quality data and the spacecraft
 31 and the simulation are in the same region. We determine the location of the bow shock,
 32 the magnetopause and the neutral sheet in the spacecraft measurements and compare
 33 their position in the observation and simulations.

34 The GUMICS–4 provides quite good results in the solar wind however its accu-
 35 racy is **worse** in the magnetosheath. The simulation results are not realistic in the mag-
 36 netosphere. The bow shock location is predicted well however the magnetopause loca-
 37 tion is less accurate. The neutral sheet positions are located quite well thanks to the spe-
 38 cial solar wind conditions. The reason for **the inaccuracy of the magnetopause po-**
 39 **sition and the parameters of the magnetosphere** is the missing inner magneto-
 40 sphere model.

41 **1 Introduction**

42 **One of the** most cost-effective way to study the interaction of the solar wind and
 43 the planetary magnetospheres (or predict the conditions of the near-Earth space) is us-
 44 ing a global magnetohydrodynamic (MHD) code. In the past, several [...] parallelized,
 45 effective, verified and validated codes were developed, which are used and applied to fore-
 46 cast the cosmic environment of the Earth; such as the Lyon-Fedder-Mobarry [LFM; *Lyon*
 47 *et al.*, 2004] code, the Open Geospace General Circulation Model [OpenGGCM; *Raeder*
 48 *et al.*, 2008], the Block-Adaptive-Tree-Solarwind-Roe-Upwind-Scheme [BATS-R-US; *Pow-*
 49 *ell et al.*, 1999; *Tóth et al.*, 2012]. In Europe only three global MHD codes were devel-
 50 oped: the Grand Unified Magnetosphere–Ionosphere Coupling Simulation [GUMICS–4;
 51 *Janhunen et al.*, 2012], the Computational Object Oriented Libraries for Fluid Dynam-

52 ics [COOLFluiD; *Lani et al.*, 2012] and the 3D resistive magnetohydrodynamic code Gor-
 53 gon [*Chittenden et al.*, 2004; *Ciardi et al.*, 2007]. The COOLFluiD is a general-purpose
 54 plasma simulation tool. The Gorgon code was developed for studying high energy, col-
 55 lisional plasma interactions and has been adapted to simulate planetary magnetospheres
 56 and their interaction with the solar wind [*Mejnertsen et al.*, 2016, 2018]. **Neither Gorg-**
 57 **gon nor COOLfluid have an ionospheric solver.** The GUMICS–4 was developed
 58 to study the solar wind-terrestrial magnetosphere interaction and its parallel version has
 59 not been available for the scientific community **because it is still in development** (see
 60 Section 2.1). These codes are available at the Community Coordinated Modelling Cen-
 61 ter (CCMC; <http://ccmc.gsfc.nasa.gov/>) hosted by the NASA Goddard Space Flight Cen-
 62 ter (GSFC) **or** the Virtual Space Weather Modelling Centre (VSWMC; <http://swe.ssa.esa.int/web/guest/kul->
 63 cmpa-federated; **requires registration for the European Space Agency (ESA)**
 64 **Space Situational Awareness (SSA) Space Weather (SWE) portal** hosted by
 65 the KU Leuven [*Poedts et al.*, 2020]. The comparison of the simulation results to space-
 66 craft and ground-based measurements is necessary to understand the abilities and fea-
 67 tures of the developed tools. The statistical study using long term global MHD runs for
 68 validation [...] of the codes seems to be a good and fruitful method. However, provid-
 69 ing long simulations is costly and time consuming hence only a few studies were done
 70 previously using much shorter simulations than a year.

71 *Guild et al.* [2008a,b] launched two months of LFM run and compared the plasma
 72 sheet properties in the simulated tail with the statistical properties of six years Geotail
 73 magnetic field and plasma observations [*Kokubun et al.*, 1994; *Mukai et al.*, 1994]. The
 74 LFM successfully reproduced the global features of the global plasma sheet in statisti-
 75 cal sense. However, there were some differences. The sheet was too cold, too dense and
 76 the bulk flow was faster than the observed plasma sheet. The LFM overestimated the
 77 ionospheric transpolar potential. The transpolar potential correlated with the speed of
 78 the plasma sheet flows. The equatorial maps of density, thermal pressure, thermal en-
 79 ergy and velocity were compared. The LFM overestimated the plasma sheet density close
 80 to the Earth and underestimated the temperature by a factor of ~ 3 . The LFM overes-
 81 timated the global average flow speed by a factor of ~ 2 . The LFM reproduced many of
 82 the climatological features of the Geotail data set. The low-resolution model underes-
 83 timated the occurrence of the fast earthward and tailward flows. Increasing the simu-

84 lation resolution resulted in the development of fast, busty flows. These flows contributed
 85 to the statistics and brought the simulations to the observations closer.

86 *Zhang et al.* [2011] [...] studied the statistics of magnetosphere-ionosphere (MI)
 87 coupling **using *Guild et al.* [2008a]’s LFM simulation above.** The polar cap po-
 88 tential and the field aligned currents (FAC), the downward Poynting flux and the vor-
 89 ticity of the ionospheric convection were compared with observed statistical averages and
 90 the Weimer05 empirical model [*Weimer*, 2005]. The comparisons showed that the LFM
 91 model produced quite accurate average distributions of the Region 1 (R1) and Region
 92 2 (R2) currents. The ionospheric Region 2 currents in the MHD simulation seemed to
 93 be originated from the diamagnetic ring current. The average LFM Region 1 and 2 cur-
 94 rents were smaller compared with the values from the Weimer05 model. The average CPCP
 95 was higher in the LFM simulation than the measurements of the SuperDARN and the
 96 Weimer05 model. The average convention pattern was quite symmetric in the LFM sim-
 97 ulation against the SuperDARN measurements and the Weimer05 model. The Super-
 98 DARN measurements and the Weimer05 model had dawn-dusk asymmetry. In the LFM
 99 model more Poynting flux flowed into the polar region ionosphere than in the Weimer05
 100 model. It was the consequence of the larger CPCP in the LFM simulation. The larger
 101 CPCP allowed higher electric field in the polar region. The statistical dependence of the
 102 high-latitude convection patterns on Interplanetary Magnetic Field (IMF) clock angle
 103 was similar to the SuperDARN measurements [*Sofko et al.*, 1995] and the Weimer05 model.
 104 The average ionospheric field-aligned vorticity showed good agreement on the dayside.
 105 However, the LFM model gave larger nightside vorticity than SuperDARN measurements
 106 because the Pedersen conductance on the night side ionosphere was too low.

107 *Wiltberger et al.* [2017] studied the structure of the high latitude field-aligned cur-
 108 rent patterns using three resolutions of the LFM global MHD code and the Weimer05
 109 empirical model [*Weimer*, 2005]. The studied period was a month long and contained
 110 two high-speed streams. Generally, the patterns agreed well with results obtained from
 111 the Weimer05 computing. As the resolution of the simulations increased, the currents be-
 112 came more intense and narrow. The ratio of the Region 1 (R1), the Region 2 (R2) cur-
 113 rents and the R1/R2 ratio increased when the simulation resolution increases. However,
 114 both the R1 and R2 currents were smaller than the predictions of the Weimer05 model.
 115 This effect led to a better agreement of the LFM simulation results with the Weimer 2005
 116 model results. The CPCP pattern became concentrated in higher latitudes because of

117 the stronger R2 currents. The relationship of the CPCP and the R1 looked evident at
 118 higher resolution of the simulation. The LFM simulation could have reproduced the sta-
 119 tistical features of the field aligned current (FAC) patterns.

120 *Hajducek et al. [2017]* simulated a month of January 2005 using the Space Weather
 121 Modelling Framework [SWMF; *Tóth et al.*, 2005] and the OMNI solar wind data as in-
 122 put. The simulations were done with and without inner magnetosphere model and us-
 123 ing two different grid resolutions. The model was very good in predicting the **ring** cur-
 124 rents [...] [SYM-H; <http://wdc.kugi.kyoto-u.ac.jp/aeasy/asy.pdf>; *Iyemori*, 1990]. The
 125 K_p index (that measures the general magnetospheric convention and the auroral currents
 126 [*Bartels et al.*, 1939; *Rostoker*, 1972; *Thomsen*, 2004]) was predicted well during storms
 127 however the index was over predicted during quiet time periods. The AL index (that de-
 128 scribes the westward electro jet of the surface magnetic field introduced by *Davis and*
 129 *Sugiura* [1966]) was predicted reasonably well in average however the model reached the
 130 highest negative AL value less often than the observations because the model captured
 131 the structure of the auroral zone currents poorly. The overpredicting of K_p index dur-
 132 ing quiet times might have had the same reason because that index was also sensitive
 133 for the auroral zone dynamics. The SWMF usually over predicted the CPCP. These re-
 134 sults were not sensitive to grid resolutions. Except that the AL index reached the high-
 135 est negative value more often when the grid resolution was higher. Switching off of the
 136 inner magnetosphere model had dramatic effect for the accuracy of all quantities men-
 137 tioned above, except the CPCP.

138 In this paper the Cluster SC3 measurements are compared directly to a previously
 139 made 1-year long GUMICS–4 simulation in the solar wind, magnetosheath and the mag-
 140 netosphere along the Cluster SC3 orbit saved from the simulation results and measured
 141 by the spacecraft [*Facskó et al.*, 2016]. Three parameters (B_z , V_X and n) were studied
 142 as well as the location of the bow shock, magnetopause and the neutral sheet. The struc-
 143 ture of this paper is as follows. Section 2 describes the GUMICS–4 code, the 1-year sim-
 144 ulation and the instruments. Section 3 gives comparisons between the simulations and
 145 observations. Results of the comparison are discussed in Section 4. Finally, Section 5 con-
 146 tains the conclusions.

147 **2 The GUMICS–4 products and Cluster measurements**

148 Here we use two [...] very different [...] time series. The first **time series are**
 149 derived from a previously made 1-year GUMICS–4 simulation [*Facskó et al.*, 2016]. The
 150 second **time series were** measured by the magnetometer, ion plasma and electric field
 151 instruments of the Cluster reference spacecraft.

152 **2.1 The GUMICS–4 code**

153 The GUMICS–4 has two coupled simulation domains, the magnetospheric domain
 154 outside of $3.7 R_E$ radius around the Earth and a coupled ionosphere module containing
 155 a 3D electron density model of the ionosphere. The GUMICS–4 is not a parallel code
 156 however it was extensively used for studying the energy propagation processes from the
 157 solar wind to the magnetosphere through the magnetopause and other features [*Janhunen*
 158 *et al.*, 2012, see the references therein]. The code has also been applied for studying the
 159 forced reconnection in the tail [*Vörös et al.*, 2014]. Recently a few hundreds of synthetic
 160 two hours duration GUMICS–4 simulations were made to compare the simulation re-
 161 sults to empirical formulas [*Gordeev et al.*, 2013]. The agreement was quite good how-
 162 ever the diameter of the magnetopause deviated significantly in the simulation and the
 163 observations in the tail. The tail of the GUMICS–4 was smaller than spacecraft observed
 164 and measured. A 1-year long simulation was made using the GUMICS–4 code [*Facskó*
 165 *et al.*, 2016]. *Juusola et al.* [2014] compared the ionospheric currents, fields and the cross
 166 polar cap potential (CPCP) in the simulation versus Super Dual Auroral Radar Network
 167 (SuperDARN) radars [*Greenwald et al.*, 1995] and CHAMP spacecraft [*Reigber et al.*,
 168 2002] field aligned currents (FAC) measurements [*Juusola et al.*, 2007; *Ritter et al.*, 2004].
 169 The agreement was good in the seasonal variation of the CPCP however the FAC and
 170 other currents could not be reproduced properly. The possible cause of this bad agree-
 171 ment could be the lack of the inner magnetosphere model. This statement is supported
 172 by the result of *Hajducek et al.* [2017]. *Hajducek et al.* simulated only a month using dif-
 173 ferent spatial resolution and to test the codes switched off the inner magnetosphere model
 174 of the SWMF for a special run. This run without inner magnetosphere model made it
 175 clear that only the CPCP parameter of the simulation agreed quite well with the mea-
 176 surement. This fact explained why the agreement between the Cluster SC3 and the GUMICS-
 177 4 simulations was so good as described by [*Lakka et al.*, 2018a,b] based on the CPCP
 178 in GUMICS–4 simulations. *Kallio and Facskó* [2015] determined the solar wind param-

eters along the Moon orbit using the results of the *Facskó et al.* [2016]’s global MHD simulations. The solar wind parameters differed significantly in the geotail that should have been considered in future studies of the interaction of the solar wind and the lunar orbit. *Facskó et al.* [2016] determined the footprint of the Cluster SC3 using the 1-year simulation and the Tsyganenko T96 empirical model [*Tsyganenko*, 1995]. The code seemed to react slower to the dynamic changes of the solar wind pressure than the empirical model. The agreement of the footprint is better in the Northern Hemisphere. The GUMICS–4 tail looked shorter in the simulations than the observations. Finally, the Y component of the interplanetary magnetic field twisted the simulated tail hence the agreement of the empirical and computational footprints was worse at such solar wind conditions.

A workpackage of the European Cluster Assimilation Technology (ECLAT) project (https://cordis.europa.eu/result/rcn/165813_en.html; <http://www.eclat-project.eu/>) was the creation and analysis of a 1-year global MHD simulation using the OMNI solar wind data from January 29, 2002 to February 2, 2003 as input of the GUMICS–4 code [*Facskó et al.*, 2016]. The GUMICS-4 was a single core system [*Janhunen et al.*, 2012] hence the 1-year simulation was made in 1860 independent runs. This interval covered 155 Cluster SC3 orbits and each orbit lasted 57 hours. The supercomputer had 12 CPUs on each node hence the 57 hours were divided into 4.7 hours simulation time with one hour initialisation period. Each sub-intervals used its own average Geocentric Solar Ecliptic (GSE) IMF magnetic field X component B_x component and dipole tilt angle. All data gaps of the input file were filled using interpolation. If the data gap of the input file was at the beginning (or the end) interval the first (or last) good data of the input file was used to fill the gap. The initialisation of each simulations was made using constant values. These values were the first valid data of the input file repeated 60 times (60 minutes) in the input file of the sub-interval. The simulation results were saved in every five minutes. Various simulation parameters, for example, the density, particle density, temperature, magnetic field, solar wind velocity (29 different quantities) were saved from the simulation results along the Cluster reference spacecraft in the GSE coordinates. In this paper these parameters, namely the B_z magnetic field GSE Z component, the solar wind velocity GSE X component (V_x) and the solar wind density n are compared to the Cluster SC3 measurement. These parameters are selected because the B_z controls the magnetosphere, the V_x is the main solar wind velocity component and the n is the ion plasma

211 momentum that is the easiest to calculate; furthermore more instruments could deter-
 212 mine it (see Section 2.2).

213 2.2 The Cluster SC3 measurements

214 The Cluster-II spacecraft of the European Space Agency (ESA) were launched in
 215 2000 and study the geospace since then [Credland *et al.*, 1997; Escoubet *et al.*, 2001]. Its
 216 four spacecraft form a tetrahedron however here we use only the measurements of the
 217 reference spacecraft, the Cluster SC3. The spacecraft were stabilised by rotation and its
 218 period is ~ 4 s. Hence, the temporal resolution of the plasma instruments were consid-
 219 ered 4 s and we use 4 s averaged magnetic field data. The real resolution of the Cluster
 220 FluxGate Magnetometer (FGM) magnetic field instrument was 27 Hz [Balogh *et al.*, 1997,
 221 2001]. The ion plasma data was provided by the Cluster Ion Spectrometry (CIS) Hot
 222 Ion Analyser (HIA) sub-instrument [Reme *et al.*, 1997; Rème *et al.*, 2001]. The CIS HIA
 223 instrument is calibrated using the Waves of HIgh frequency Sounder for Probing the Elec-
 224 tron density by Relaxation (WHISPER) wave instrument onboard Cluster [Décréau *et al.*,
 225 2001; Trotignon *et al.*, 2010; Blagau *et al.*, 2013, 2014]. These calibrations might have
 226 appeared as sudden non-physical jumps in the CIS HIA data. The CIS HIA had differ-
 227 ent modes to measure in the solar wind and the magnetosphere. When the instrument
 228 switched from a mode to another mode it appeared as a non-physical jump in the mea-
 229 sured data too. These features had an influence on the accuracy of the data analysis.

230 We protect our results from these non-physical jumps described previously using
 231 a density determination based on different principles. We use the spacecraft potential
 232 of the Electric Field and Wave Experiment [EFW ; Gustafsson *et al.*, 1997, 2001] to de-
 233 termine the electron density. This quantity can be calculated using the empirical den-
 234 sity formula

$$n_{EFW} = 200(V_{sc})^{-1.85}, \quad (1)$$

235 where n_{EFW} is the calculated density and V_{sc} is the Cluster EFW spacecraft potential
 236 [Trotignon *et al.*, 2010, 2011]. The EFW and the WHISPER were used for the calibra-
 237 tion of the CIS HIA and the Plasma Electron and Current Experiment [PEACE; John-
 238 stone *et al.*, 1997; Fazakerley *et al.*, 2010a,b]. Both instruments were still working on-
 239 board all Cluster spacecraft. Their stable operation reduced the number of data gaps;
 240 furthermore made the data analysis easier.

241 **3 Comparison of measurements to simulation**

242 The saved parameters from the GUMICS–4 simulations and the Cluster SC3 mag-
 243 netic field, solar wind velocity and density measurements are compared in the solar wind,
 244 magnetosheath and magnetosphere using cross correlation calculation. The resolution
 245 of the simulated Cluster orbit data is mostly five minutes because the simulations are
 246 saved in every five minutes [Facsikó *et al.*, 2016]. However, the time difference between
 247 points could be more than five minutes at the boundary of the subintervals, because the
 248 length of simulation intervals is determined in minutes. To facilitate analysis of the sim-
 249 ulation results, all simulation data were interpolated to one minute resolution. This method
 250 does not provide extra information to the cross correlation calculation. The data gaps
 251 are eliminated using interpolation in the data and extrapolation when the gap is at the
 252 start or the end of the selected interval. The spin resolution (4 s) of Cluster SC3 mag-
 253 netic field measurements is averaged over one minute around ($\pm 30\text{ s}$) the time stamps
 254 of the saved data.

255 For the correlation calculation intervals are selected carefully in the solar wind (see
 256 **Section 3.1**), the magnetosheath (see **Section 3.2**), the dayside and the night side mag-
 257 netosphere (see **Section 3.3**). In these intervals the parameters did not vary a lot and
 258 neither the Cluster nor the virtual probe crossed any boundary layers. To compare the
 259 shape of the B_z magnetic field, V_x solar wind speed and the n_{CIS} and the n_{EFW} curves
 260 we calculate cross correlation on selected intervals. Sometimes we get very bad results.
 261 Then we carefully examined the case and remove the short intervals (shorter than four
 262 hours) from the correlation calculation and large data gaps from the correlation calcu-
 263 lation. (The data gaps are interpolated however they cause loss of information.) Those
 264 intervals are also neglected where the plasma instrument has a calibration error or changes
 265 its mode from magnetosphere to solar wind (for example). The electron density is also
 266 calculated using the empirical density formula (see Equation 1) and making the corre-
 267 lation calculation. We want to avoid calibration errors and sudden non-physical jumps
 268 mentioned previously. The results do not differ significantly however the n_{EFW} does not
 269 have any mode change and it is applicable in the magnetosphere too (against the CIS
 270 HIA instrument).

271 **3.1 Solar wind**

272 We use OMNI IMF and solar wind velocity, density and temperature data as input
 273 of the simulation. Nevertheless, it is not useless to compare the solar wind region
 274 in the simulation and the measurements. The IMF X component cannot be given to the
 275 GUMICS–4 as input [Janhunen *et al.*, 2012; Fácskó *et al.*, 2016]. However the magnetic
 276 field of the solar wind has X component in the simulations. Additionally the solar wind
 277 structure might change from the simulation domain boundary at $+32 R_E$ to the sub-solar
 278 point of the terrestrial bow shock where all OMNI data is shifted. Almost the same so-
 279 lar wind intervals are used as in the see Table 1 of Fácskó *et al.* [2016]. The number of
 280 these intervals is small because the Cluster fleet instruments were calibrated in 2002, just
 281 after launching (Table 1). Hence we do not have a satisfactory ion plasma data cover-
 282 age for this year. Additionally, to improve the accuracy of the correlation calculation (see
 283 below) we delete the intervals that were too short (shorter than five hours) or the CIS
 284 HIA instrument changed its mode. The Cluster fleet is located in the solar wind only
 285 from December to May and only for a couple of hours during each orbit near to the apogee.
 286 We double check whether the Cluster SC3 stays in the solar wind in both the simula-
 287 tion and reality. We also check the omnidirectional CIS HIA ion spectra on the Clus-
 288 ter Science Archive (CSA; <https://www.cosmos.esa.int/web/csa/csds-quicklook-plots>).
 289 Hence 17 intervals are left in the solar wind to study (Figure 1).

290 The selected intervals have quiet solar wind conditions (Figure 2). The GUMICS–4
 291 simulation results have five minutes resolution and the Cluster SC3 measurements have
 292 one minute resolution (Figure 3). The measurements vary significantly. In spite of the
 293 quiet conditions the solar wind density often changes and deviates from the simulation.
 294 On Figure 4c both densities deviate significantly. The CIS HIA density deviation is larger
 295 as it is expected because of the complexity and the large number of working modes of
 296 the CIS instrument. The magnetic field and the solar wind velocity fit better. On Fig-
 297 ure 5a the correlation of the magnetic field is very good; furthermore on Figure 5c, 5e, 5f
 298 the correlation of the solar wind velocity and density is excellent (Table 1). The time
 299 shift on Figure 5b, Figure 5d, Figure 5f is about five minutes for the magnetic field and
 300 the CIS data. On Figure 5h for the EFW data the time shift is worse. It is not deter-
 301 mined as well as the other parameters.

302 **3.2 Magnetosheath**

303 The Cluster SC3 spent only a little time in the solar wind from December, 2002
 304 to May, 2003. However, the orbit of the spacecraft always crosses the magnetosheath (Figure 6). We selected intervals when the value of the magnetic field is around 25 nT. The
 305 field should be fluctuating because of the turbulent and deviated flow of the solar wind
 306 after passing the bow shock. In the same time the solar wind temperature increases. The
 307 solar wind speed drops hence its value is only 100-300 km/s. The density of the plasma
 308 flow increased and reached the $10\text{-}20 \text{ cm}^{-3}$. The narrow band on the omnidirectional CIS
 309 HIA ion spectra from the CSA (<https://www.cosmos.esa.int/web/csa/csds-quicklook-plots>) is widened after passing the bow shock. 15–30 minutes after this crossing we con-
 310 sidered the Cluster SC3 to enter into the magnetosheath. At the inner boundary **of the**
 311 **magnetopause** the flow speed drops and the density as well. The magnetic field starts
 312 growing and it is less turbulent than in the magnetosheath. The wide band on the the
 313 omnidirectional CIS HIA ion spectra disappears. 15–30 minutes before the appearance
 314 of these indicators of the magnetopause crossing our intervals end. All intervals contain
 315 large data gap, non-physical jump of instrument mode changing or shorter than four hour
 316 are removed. Hence 74 intervals considered in our final selection (Table 2).

319 All intervals have quiet upstream (or input) solar wind conditions (Figure 7). In
 320 [...] our selections the magnetic field and the plasma parameters and the calculated
 321 empirical density vary significantly stronger than in the solar wind intervals (Figure 8).
 322 The deviation of the simulated and the observed data is larger in this region as well. The
 323 scattered plots of the magnetic field, plasma flow speed and the densities agree well how-
 324 ever these plots are relatively less accurate than the scattered plots of the solar wind (Fig-
 325 ure 9a, 9b, 9c). The correlation of the simulated and the observed data is good for the
 326 magnetic field (Figure 10a), very good for the ion plasma moments and the calculated
 327 density (Figure 10c, 10e, 10g). The timeshift of the magnetic field is within five min-
 328 utes mostly (Figure 10b) however the timeshift of the ion plasma moments is scattered
 329 (Figure 10d, 10f). The timeshift of the calculated EFW density seems to be more ac-
 330 curate (Figure 10h). Generally, the GUMICS–4 is less accurate in the magnetosheath.
 331 **The modelled magnetic field is closer to the observations than the modelled**
 332 **plasma parameters are.** The calculated empirical EFW density (n_{EFW}) fits better
 333 than the CIS HIA density (n_{CIS}).

334 **3.3 Magnetosphere**

335 To select intervals in the magnetosphere we looked for the CIS HIA **omnidirectional**
 336 ionflux **spectrum**. Where the band of the hot magnetosheath ion population (dis)appeared,
 337 the magnetosphere started/finished. The solar wind density slowly becomes zero, the mag-
 338 netic field and the solar wind density drop and reach the zero value. We left 15–30 min
 339 after/before the magnetopause transition to appoint the interval in the magnetosphere.
 340 This way we found 132 intervals in the magnetosphere (Table 3) using Cluster SC3 mea-
 341 surements. The Cluster SC3 spends considerable time in the magnetosphere (Figure 11).

342 Here we show neither any correlation calculation nor comparison plot. In the mag-
 343 netosphere the GUMICS–4 does not work well. Neither the magnetic field nor the plasma
 344 moments nor the N_{EFW} fit well. The solar wind velocity does not reach zero in the sim-
 345 ulation. Instead the solar wind enters to the night side magnetosphere. The solar wind
 346 CIS HIA ion plasma density and the calculated density from spacecraft potential increase
 347 closer to the Earth (plasmasphere). The GUMICS–4 density is low there. We calculated
 348 the dipole field in GSE using Tsyganenko geotool box [Tsyganenko, 1995] and substracted
 349 from both the observed and the simulated magnetic field B_z data. The correlation of these
 350 corrected magnetic field measurements and simulations is very low too.

351 **3.4 Bow shock, magnetopause, neutral sheet**

352 77 intervals are selected when the Cluster SC3 crossed the terrestrial bow shock
 353 once or multiple times (**Table 6**). When the spacecraft crosses the bow shock inwards
 354 the magnitude of the magnetic field and the solar wind density increases 4–5 times (from
 355 5 nT or 5 cm^{-3} , respectively), the solar wind speed drops from 400–600 km/s to 100–300 km/s;
 356 furthermore the narrow band on the omnidirectional Cluster CIS HIA ion spectra is widened.
 357 The Cluster measurements are 1-min averaged and the GUMICS–4 simulations has 5-
 358 min resolution hence all bow shock transitions of the virtual spacecraft are slower and
 359 smoother. Additionally, the multiple bow shock transitions are not visible in the GUMICS
 360 simulations. The code reacts slowly for such sudden changes. The magnetic signatures
 361 fit better than the calculated plasma moments. The jump of the ion plasma parameters
 362 and the derived Cluster EFW density of the simulations are shifted to the measurements.
 363 Generally, the density and the velocity of the simulations seem to be less accurate than
 364 the magnetic field of the simulations.

54 intervals are selected around magnetopause crossings [...] (**Table 7**). When the spacecraft crosses the magnetopause inward direction the magnitude of the magnetic field increases, the solar wind speed drops from 100–300 km/s to zero, the plasma density becomes zero; furthermore the wide band on the omnidirectional Cluster CIS HIA ion spectra disappears. These changes are not that fast. The location of the magnetopause is well determined by the Cluster SC3 measurements. However, it is very difficult to identify the magnetopause crossings in the simulation data. [...] The magnetopause crossings very often cannot be seen in the simulations. Or when the magnetopause crossings are clearly identified in both simulations and spacecraft measurements the events are shifted. The accuracy of the model is lower for the dayside magnetopause locations.

Nine intervals are chosen around Cluster SC3 neutral sheet crossings (Figure 12; Table 8). The neutral sheets location is determined using the results of the Boundary Layet Identification Code (BLIC) Project [Facsikó *et al.*, in preparation]. The BLIC code determines the neutral sheet crossing Cluster FGM magnetic field measurements using Wang and Xu [1994]’s method. When the solar wind speed is almost zero; furthermore the CIS HIA density and the EFW calculated density are almost zero too; finally the GSE Z component of the magnetic field changes is a sign of the code indicated neutral sheet crossing (Figure 20; red and blue curves). Surprisingly the neutral sheet crossings are visible very well in the GUMICS simulations (Figure 20; black curves). For five events (from nine Cluster SC3 crossings) the GUMICS–4 also provides similar smoothed parameters and change of sign of the B_z component. This is a **outstanding** result because the tail in the GUMICS–4 simulations is significantly smaller than the observed reality [Gordeev *et al.*, 2013; Facsikó *et al.*, 2016]; furthermore the solar wind enters the tail in MHD simulations generally [Kallio and Facsikó, 2015].

4 Discussion

The agreement of the solar wind B_z , V_x and n_{EFW} with the similar GUMICS simulation parameters is very good (Figure 4a, 4b, 4c, blue). The agreement of the n_{CIS} is worse (Figure 4c, red). It was expected because the n_{EFW} depends on the spacecraft potential provided by the EFW instrument. However, the CIS instrument has many modes for measuring the plasma parameters and it needs periodical calibration too. The correlation of the solar wind V_x , n_{CIS} and n_{EFW} with the similar GUMICS simulation parameters is greater than 0.9 (Figure 5c, 5e, 5g). The correlation of the B_z is also greater

than 0.8 (Figure 5a). Both numbers prove very high correlation. The inbound wall of
 the GUMICS–4 code is at $32 R_E$ [Janhunen et al., 2012], the nose of the terrestrial bow
 shock is at about $20 R_E$. If the solar wind speed is 400 km/s, then this spatial distance
 means less than 5 minutes delay, so it should not be visible. 80% of the intervals sup-
 port this theory but 20 % not. In these cases the one-minute resolution B_z , n_{CIS} or the
 n_{EFW} parameters have a sudden jump or variation that the simulation cannot follow,
 or the resolution of the simulation data (5 minutes) is too small to see these variations.
 Therefore, the correlation calculation is not accurate in these cases. Previously the OMNI
 data was compared to the Cluster data and the Cluster measurements were compared
 to the GUMICS–4 [Facsikó et al., 2016]. The comparison suggests that the GUMICS–4
 results should be similar with the OMNI data. Furthermore, we calculate correlation func-
 tions in the solar wind, where there is no significant perturbation of the input param-
 eters in the simulation box. Therefore, we get an expected result after comparing the
 two different correlation calculations.

In the magnetosheath we get worse agreement with the GUMICS simulation data
 (Figure 9a, 9b, 9c). However, it just means a larger uncertainty of the scattered plot.
 The general reason of this larger uncertainty seems to be the larger number of points.
 The slowed down solar wind shows strong turbulence. This phenomena explains the higher
 variations of the B_z magnetic field on Figure 9a. The solar wind V_x , n_{CIS} and n_{EFW}
 agree better than the magnetic field component (Figure 9b, 9c). Here there is no devi-
 ation between the densities derived in different ways (n_{CIS} and n_{EFW}) on Figure 9c.
 Figure 10 seems to contradict these statements above. The larger uncertainty of the B_z
 is visible on Figure 10a. However, that correlation is still good on Figure 10b. The other
 parameters have larger (> 0.9) correlation on Figure 10c, 10e, 10g. However, the time
 shifts on Figure 10d, 10f, 10h seem to be worse. Actually here the time shifts are worse
 because the shape of the time series in the magnetosheath looks very similar. Hence, the
 correlation calculation provides larger time shifts for the ion plasma parameters and the
 n_{EFW} .

In the magnetosphere the GUMICS–4 does not work well. The GUMICS–4 uses
 a tilted dipole to describe the terrestrial magnetic field [Janhunen et al., 2012]. After re-
 moving the magnetic dipole from the magnetic field measurements of the Cluster SC3
 and the simulation we get very low correlations and unacceptable time shifts (not shown).
 In the inner magnetosphere the tilted dipole is an insufficient description. However, the

430 plasma momentums and the n_{EFW} do not fit either. The MHD approach lost its validity
 431 in the inner magnetosphere domain therefore the V_x and the n of the simulations do
 432 not agree to the V_x , the n_{CIS} and the n_{EFW} measured by the Cluster SC3. Within the
 433 3.7 R_E domain another model is necessary that contains more physics as you can see it
 434 in other global MHD codes [Lyon *et al.*, 2004; Raeder *et al.*, 2008; Powell *et al.*, 1999;
 435 Tóth *et al.*, 2012]. This result explains the limited accuracy of the cross polar cap po-
 436 tential (CPCP) and geomagnetic indices of the GUMICS simulations [Juusola *et al.*, 2014].
 437 The CPCP had good agreement of GUMICS simulations and spacecraft measurements
 438 therefore this quantity could be used for capable and relevant simulation studies [Lakka
 439 *et al.*, 2018a]. Haiducek *et al.* [2017] also made a comparison study of the geomagnetic
 440 indices and the CPCP. The Space Weather Modelling Framework (SWMF) was tested.
 441 When the inner magnetosphere model was switched off in the simulation only the com-
 442 parison of the simulated and observed CPCP was good. Therefore, the reason of the dis-
 443 crepancy of the geomagnetic indices in the GUMICS simulations must be the missing
 444 inner magnetosphere model.

445 The reason of the disagreement of the simulation results and the measurements could
 446 be the code or the bad input parameters. During the 1-year run the distributions of the
 447 OMNI solar wind magnetic field B_x , B_y , B_z components (Figure 13a, 13b, 13c); solar
 448 wind velocity V_x , V_y V_z components (Figure 13d, 13e, 13f) and the solar wind P dynamic
 449 pressure are calculated (Figure 13g) from January 29, 2002 to February 2, 2003 in GSE
 450 reference frame. The intervals when the GUMICS–4 simulations and the Cluster SC3
 451 measurements disagreed are collected for intervals in the solar wind (Table 4) and the
 452 magnetosheath (Table 5). The averaged shifted OMNI parameters of the poorly agree-
 453 ing intervals from the Tables 4 and 5 are saved. The distributions of the OMNI param-
 454 eters belonging to the bad simulation results are calculated for the solar wind region (Fig-
 455 ure 14, 15 and 16) and in the magnetosheath (Figure 17, 18 and 19). In the solar wind
 456 the distributions of the OMNI B_x , B_y and B_z can be compared on Figure 13a and Fig-
 457 ure 14a, 14d, 14g, 14j; Figure 13b and Figure 14b, 14e, 14h, 14k; furthermore on Fig-
 458 ure 13c and Figure 14c, 14f, 14i, 14l. When the V_x disagrees in simulations and measure-
 459 ments on Figure 14d, 14e, 14f the distributions of the OMNI B_x , B_y and B_z are simi-
 460 lar to the distributions of the OMNI B_x , B_y and B_z on Figure 13a, 13b and 13c. When
 461 the n_{CIS} disagrees in simulations and measurements on Figure 14g, 14h, 14i the distri-
 462 butions of the OMNI B_x , B_y and B_z are similar to the distributions of the OMNI B_x ,

463 B_y and B_z on Figure 13a, 13b and 13c. When the n_{EFW} disagrees on Figure 14j, 14k, 14l
 464 the distributions of the OMNI B_x , B_y and B_z are similar to the distributions of the OMNI
 465 B_x , B_y and B_z on Figure 13a, 13b and 13c. The distributions do not agree perfectly be-
 466 cause in Table 4 the number of the poorly correlated intervals is only 6, 12 and 9 for the
 467 V_x , the n_{CIS} and n_{CIS} components, respectively. When the B_z disagrees in simulations
 468 and measurements on Figure 14a, 14b, 14c the distributions of the OMNI B_x , B_y and
 469 B_z are not similar to the distributions of the OMNI B_x , B_y and B_z on Figure 13a, 13b
 470 and 13c. The values of the OMNI B_x , B_y and B_z are not peculiar in the solar wind. The
 471 reason of these strange spikes is that there is only one poorly correlated interval for the
 472 B_z in the solar wind according to Table 4. In the solar wind the distributions of the OMNI
 473 V_x , V_y and V_z can be compared on Figure 13d and Figure 15a, 15d, 15g, 15j; Figure 13e
 474 and Figure 15b, 15e, 15h, 15k; furthermore on Figure 13f and Figure 15c, 15f, 15i, 15l.
 475 When the V_x disagrees in simulations and measurements on Figure 15d, 15e, 15f the dis-
 476 tributions of the OMNI V_x , V_y and V_z are similar to the distributions of the OMNI V_x ,
 477 V_y and V_z on Figure 13d, 13e and 13f. When the n_{CIS} disagrees on Figure 15g, 15h, 15i
 478 the distributions of the OMNI V_x , V_y and V_z are similar to the distributions of the OMNI
 479 V_x , V_y and V_z on Figure 13d, 13e and 13f. When the n_{EFW} disagrees in simulations and
 480 measurements on Figure 15j, 15k, 15l the distributions of the OMNI V_x , V_y and V_z are
 481 similar to the distributions of the OMNI V_x , V_y and V_z on Figure 13d, 13e and 13f. The
 482 distributions do not agree perfectly because in Table 4 the number of the poorly corre-
 483 lated intervals is only 6, 12 and 9 for the V_x , the n_{CIS} and n_{CIS} components, respec-
 484 tively. When the B_z disagrees on Figure 15a, 15b, 15c the distributions of the OMNI V_x ,
 485 V_y and V_z are not similar to the distributions of the OMNI V_x , V_y and V_z on Figure 13d, 13e
 486 and 13f. The values of the OMNI V_x , V_y and V_z are not peculiar in the solar wind. The
 487 reason of these strange spikes is that there is only one poorly correlated interval for the
 488 B_z in the solar wind according to Table 4. In the solar wind the distributions of the OMNI
 489 P can be compared on Figure 13g and Figure 16a, 16b, 16c, 16d. When the V_x disagrees
 490 in simulations and measurements on Figure 16b the distribution of the OMNI P is sim-
 491 ilar to the distributions of the OMNI P on Figure 13g. When the n_{CIS} disagrees in sim-
 492 ulations and measurements on Figure 16c the distribution of the OMNI P is similar to
 493 the distributions of the OMNI P on Figure 13g. When the n_{EFW} disagrees in simula-
 494 tions and measurements on Figure 16d the distribution of the OMNI P is similar to the
 495 distributions of the OMNI P on Figure 13g. The distributions do not agree perfectly be-

cause in Table 4 the number of the poorly correlated intervals is only 6, 12 and 9 for the V_x , the n_{CIS} and n_{CIS} components, respectively. When the B_z disagrees on Figure 16a the distribution of the OMNI P is not similar to the distribution of the OMNI P on Figure 13g. The values of the OMNI P are not peculiar in the solar wind. The reason of these strange spike is that there is only one poorly correlated interval for the B_z in the solar wind according to Table 4. In the magnetosheath the distributions of the OMNI B_x , B_y and B_z can be compared on Figure 13a and Figure 17a, 17d, 17g, 17j; Figure 13b and Figure 17b, 17e, 17h, 17k; furthermore on Figure 13c and Figure 17c, 17f, 17i, 17l. When the B_z disagrees in simulations and measurements on Figure 17a, 17b, 17c the distributions of the OMNI B_x , B_y and B_z are similar to the distributions of the OMNI B_x , B_y and B_z on Figure 13a, 13b and 13c. When the V_x disagrees in simulations and measurements on Figure 17d, 17e, 17f the distributions of the OMNI B_x , B_y and B_z are similar to the distributions of the OMNI B_x , B_y and B_z on Figure 13a, 13b and 13c. When the n_{CIS} disagrees in simulations and measurements on Figure 17g, 17h, 17i the distributions of the OMNI B_x , B_y and B_z are similar to the distributions of the OMNI B_x , B_y and B_z on Figure 13a, 13b and 13c. When the n_{EFW} disagrees on Figure 17j, 17k, 17l the distributions of the OMNI B_x , B_y and B_z are similar to the distributions of the OMNI B_x , B_y and B_z on Figure 13a, 13b and 13c. The distributions agree quite well because in Table 5 the number of the poorly correlated intervals 18, 50, 33 and 30 for the B_z , the V_x , the n_{CIS} and n_{CIS} components, respectively. The number of cases are higher and the values of the OMNI B_x , B_y and B_z are not peculiar in the magnetosheath. In the magnetosheath the distributions of the OMNI V_x , V_y and V_z can be compared on Figure 13d and Figure 18a, 18d, 18g, 18j; Figure 13e and Figure 18b, 18e, 18h, 18k; furthermore on Figure 13f and Figure 18c, 18f, 18i, 18l. When the B_z disagrees on Figure 18a, 18b, 18c the distributions of the OMNI V_x , V_y and V_z are similar to the distributions of the OMNI V_x , V_y and V_z on Figure 13d, 13e and 13f. When the V_x disagrees in simulations and measurements on Figure 18d, 18e, 18f the distributions of the OMNI V_x , V_y and V_z are similar to the distributions of the OMNI V_x , V_y and V_z on Figure 13d, 13e and 13f. When the n_{CIS} disagrees on Figure 18g, 18h, 18i the distributions of the OMNI V_x , V_y and V_z are similar to the distributions of the OMNI V_x , V_y and V_z on Figure 13d, 13e and 13f. When the n_{EFW} disagrees in simulations and measurements on Figure 18j, 18k, 18l the distributions of the OMNI V_x , V_y and V_z are similar to the distributions of the OMNI V_x , V_y and V_z on Figure 13d, 13e and 13f. The distributions agree quite well because in

529 Table 5 the number of the poorly correlated intervals 18, 50, 33 and 30 for the B_z , the
 530 V_x , the n_{CIS} and n_{CIS} components, respectively. The number of cases are higher and
 531 the values of the OMNI V_x , V_y and V_z are not peculiar in the magnetosheath. In the mag-
 532 netosheath the distributions of the OMNI P can be compared on Figure 13g and Fig-
 533 ure 19a, 19b, 19c, 19d. When the B_z disagrees on Figure 19a the distribution of the OMNI
 534 P is similar to the distribution of the OMNI P on Figure 13g. When the V_x disagrees
 535 in simulations and measurements on Figure 19b the distribution of the OMNI P is sim-
 536 ilar to the distributions of the OMNI P on Figure 13g. When the n_{CIS} disagrees in sim-
 537 ulations and measurements on Figure 19c the distribution of the OMNI P is similar to
 538 the distributions of the OMNI P on Figure 13g. When the n_{EFW} disagrees in simula-
 539 tions and measurements on Figure 19d the distribution of the OMNI P is similar to the
 540 distributions of the OMNI P on Figure 13g. The distributions do not agree perfectly be-
 541 cause in Table 5 the number of the poorly correlated intervals is only 6, 12 and 9 for the
 542 V_x , the n_{CIS} and n_{CIS} components, respectively. The distributions agree quite well be-
 543 cause in Table 5 the number of the poorly correlated intervals 18, 50, 33 and 30 for the
 544 B_z , the V_x , the n_{CIS} and n_{CIS} components, respectively. The number of cases are higher
 545 and the values of the OMNI P are not peculiar in the magnetosheath. The inaccuracy
 546 of the GUMICS-4 simulations does not depend on the OMNI parameters in the solar wind
 547 and magnetosheath regions. The same study does not need to be done for the magne-
 548 tosphere because the deviance of the measurements and the simulations is so large that
 549 it cannot be caused by the wrong OMNI solar wind parameters.

550 The bow shock positions agree in the GUMICS simulations and the Cluster SC3
 551 measurements. However, the magnetopause locations do not fit as good as the bow shock
 552 in simulations and observations. In simulations the location of the magnetopause is de-
 553 termined by **the downwind extension of the solar wind stagnation streamline**
 554 (**so-called fluopause**), **the maximum of the GSE Y component of the currents**
 555 density or particle density gradient [Siscoe *et al.*, 2001; García and Hughes, 2007; Gordeev
 556 *et al.*, 2013, see references therein]. In this paper the previously saved simulation param-
 557 eters along the virtual Cluster SC3 orbit are analysed. Therefore, the above mentioned
 558 methods cannot be applied. The reason of the inaccuracy of the magnetopause positions
 559 in the simulations must be the missing inner magnetosphere and ring current module.
 560 This discrepancy of the magnetopause location agrees with the results of Gordeev *et al.*
 561 [2013] and Facskó *et al.* [2016]. Gordeev *et al.* [2013] compared synthetic GUMICS runs

562 with empirical formula of the magnetopause locations. *Facskó et al.* [2016] used OMNI
 563 solar wind data as input and got the same result as *Gordeev et al.* [2013] and this pa-
 564 per. Surprisingly the neutral sheets are visible in both simulations and observations (Fig-
 565 ure 20, Table 8). This experience is exceptional because the night side magnetosphere
 566 of the GUMICS–4 simulations is small and twisted [*Gordeev et al.*, 2013; *Facskó et al.*,
 567 2016]. However, in these cases the IMF has no large B_y component. From *Facskó et al.*
 568 [2016] we know that the GUMICS has normal long tail (or night side magnetosphere)
 569 if the B_y is small.

570 5 Summary and conclusions

571 Based on the previously created 1-year long GUMICS–4 run global MHD simu-
 572 lation results are compared with Cluster SC3 magnetic field, solar wind velocity and den-
 573 sity measurements along the spacecraft orbit. Intervals are selected when the Cluster SC3
 574 and the virtual space probe are situated in the solar wind, magnetosheath and the mag-
 575 netosphere and their correlation are calculated. Bow shock, magnetopause and neutral
 576 sheet crossings are selected and their visibility and relative position are compared. We
 577 achieved the following results:

- 578 1. In the solar wind the agreement of the B_z , the V_x and the n_{EFW} is very good, fur-
 579 thermore the agreement of the n_{CIS} is also good.
- 580 2. In the magnetosheath the agreement of the magnetic field component, the ion plasma
 581 moments and the calculated empirical density is a bit worse than in the solar wind.
 582 The V_x , the n_{EFW} and the n_{CIS} fits better than the B_z component in the mag-
 583 netosheath. Their agreement is still good. The reason of the deviation is the tur-
 584 bulent behavior of the slowed down and termalised turbulent solar wind.
- 585 3. In neither the dayside nor the nightside magnetosphere can the GUMICS–4 pro-
 586 vide realistic results. The simulation outputs and the spacecraft measurement dis-
 587 agree in this region. The reason of this deviation must be the missing coupled in-
 588 ner magnetosphere model. The applied tilted dipole approach is not satisfactory
 589 in the magnetosphere at all.
- 590 4. The GUMICS–4 code causes the deviations between the simulations and the space-
 591 craft measurements because the upstream solar wind conditions seem to be nor-
 592 mal when the disagreement of the different kinds of time series is large.

593 5. The position of the bow shock and the neutral sheet agrees well in the simulations
 594 and the Cluster SC3 magnetic field, ion plasma moments and derived electron den-
 595 sity measurements in this study. The position of the magnetopause does not fit
 596 that well. The reason of this latest discrepancy must be the missing coupled in-
 597 ner magnetosphere model too.

598 The GUMICS–4 has incredible scientific and strategic importance for the European Space
 599 Weather and Scientific community. This code developed in the Finnish Meteorological
 600 Institute is the most developed and tested, widely used tool for modelling the cosmic en-
 601 viroment of the Earth in the old continent. Since the 1-year run was made some bugs
 602 of the code were fixed and the parallel version (the GUMICS–5) was developed (Honko-
 603 nen, private communication) however the parallel GUMICS is not been available on the
 604 CCMC or the VSWMC yet. We believe that the scientific community will have access
 605 to the new version and an inner magnetosphere model will be two way coupled to the
 606 existing configuration of the simulation tool.

607 Acknowledgments

608 The OMNI data were obtained from the GSFC/SPDF OMNIWeb interface at <http://omniweb.gsfc.nasa.gov>.
 609 The authors thank the FGM Team (PI: Chris Carr), the CIS Team (PI: Iannis Dandouras),
 610 the WHISPER Team (PI: Jean-Louis Rauch), the EFW Team (PI: Mats Andre) and the
 611 Cluster Science Archive for providing FGM magnetic field, CIS HIA ion plasma and WHIS-
 612 PER electron density measurements. Data analysis was partly done with the QSAS sci-
 613 ence analysis system provided by the United Kingdom Cluster Science Centre (Impe-
 614 rial College London and Queen Mary, University of London) supported by the Science
 615 and Technology Facilities Council (STFC). Eija Tanskanen acknowledges financial sup-
 616 port from the Academy of Finland for the ReSoLVE Centre of Excellence (project No. 272157).
 617 Gábor Facskó thanks Anna-Mária Vígh for improving the English of the paper. The au-
 618 thors thank Pekka Janhunen for developing the GUMICS–4 code; furthermore Minna
 619 Palmroth and Zoltán Vörös for the useful discussions. The work of Gábor Facskó was
 620 supported by mission science funding for the Van Allen Probes mission, the American
 621 Geophysical Union and the HAS Research Centre for Astronomy and Earth Sciences,
 622 Sopron, Hungary. For further use of the year run data, [...] **request the authors or**
 623 use the archive of the Community Coordinated Modelling Center (<https://ccmc.gsfc.nasa.gov/publications/posted>)

624

625 **References**

- 626 Balogh, A., M. W. Dunlop, S. W. H. Cowley, D. J. Southwood, J. G. Thomlinson,
 627 K. H. Glassmeier, G. Musmann, H. Luhr, S. Buchert, M. H. Acuna, D. H. Fair-
 628 field, J. A. Slavin, W. Riedler, K. Schwingenschuh, and M. G. Kivelson (1997),
 629 The Cluster Magnetic Field Investigation, *Space Science Reviews*, 79, 65–91, doi:
 630 10.1023/A:1004970907748.
- 631 Balogh, A., C. M. Carr, M. H. Acuña, M. W. Dunlop, T. J. Beek, P. Brown,
 632 K. Fornaçon, E. Georgescu, K. Glassmeier, J. Harris, G. Musmann, T. Oddy, and
 633 K. Schwingenschuh (2001), The Cluster Magnetic Field Investigation: overview of
 634 in-flight performance and initial results, *Annales Geophysicae*, 19, 1207–1217.
- 635 Bartels, J., N. H. Heck, and H. F. Johnston (1939), The three-hour-range index mea-
 636 suring geomagnetic activity, *Terrestrial Magnetism and Atmospheric Electricity*
 637 (*Journal of Geophysical Research*), 44, 411, doi:10.1029/TE044i004p00411.
- 638 Blagau, A., I. Dandouras, A. Barthe, S. Brunato, G. Facskó, and V. Constanti-
 639 nescu (2013), In-flight calibration of Hot Ion Analyser onboard Cluster, *Geo-*
 640 *scientific Instrumentation, Methods and Data Systems Discussions*, 3, 407–435,
 641 doi:10.5194/gid-3-407-2013.
- 642 Blagau, A., I. Dandouras, A. Barthe, S. Brunato, G. Facskó, and V. Constantinescu
 643 (2014), In-flight calibration of the Hot Ion Analyser on board Cluster, *Geoscientific*
 644 *Instrumentation, Methods and Data Systems*, 3, 49–58, doi:10.5194/gi-3-49-
 645 2014.
- 646 Chittenden, J. P., S. V. Lebedev, C. A. Jennings, S. N. Bland , and A. Ciardi
 647 (2004), X-ray generation mechanisms in three-dimensional simulations of wire
 648 array Z-pinches, *Plasma Physics and Controlled Fusion*, 46(12B), B457–B476,
 649 doi:10.1088/0741-3335/46/12B/039.
- 650 Ciardi, A., S. V. Lebedev, A. Frank, E. G. Blackman, J. P. Chittenden, C. J. Jen-
 651 nings, D. J. Ampleford, S. N. Bland, S. C. Bott, J. Rapley, G. N. Hall, F. A.
 652 Suzuki-Vidal, A. Marocchino, T. Lery, and C. Stehle (2007), The evolution of
 653 magnetic tower jets in the laboratory, *Physics of Plasmas*, 14(5), 056,501–056,501,
 654 doi:10.1063/1.2436479.
- 655 Credland, J., G. Mecke, and J. Ellwood (1997), The Cluster Mission: ESA'S
 656 Spacefleet to the Magnetosphere, *Space Science Reviews*, 79, 33–64, doi:
 657 10.1023/A:1004914822769.

- 658 Davis, T. N., and M. Sugiura (1966), Auroral electrojet activity index AE and its
659 universal time variations, *Journal of Geophysical Research*, *71*, 785–801, doi:
660 10.1029/JZ071i003p00785.
- 661 Décréau, P. M. E., P. Fergeau, V. Krasnoselskikh, E. Le Guiriec, M. Lévéque,
662 P. Martin, O. Randriamboarison, J. L. Rauch, F. X. Sené, H. C. Séran, J. G.
663 Trotignon, P. Canu, N. Cornilleau, H. de Féraudy, H. Alleyne, K. Yearby, P. B.
664 Mögensen, G. Gustafsson, M. André, D. C. Gurnett, F. Darrouzet, J. Lemaire,
665 C. C. Harvey, P. Travnicek, and Whisper Experimenters Group (2001), Early re-
666 sults from the Whisper instrument on Cluster: an overview, *Annales Geophysicae*,
667 *19*, 1241–1258, doi:10.5194/angeo-19-1241-2001.
- 668 Escoubet, C. P., M. Fehringer, and M. Goldstein (2001), Introduction The Cluster
669 mission, *Annales Geophysicae*, *19*, 1197–1200, doi:10.5194/angeo-19-1197-2001.
- 670 Facskó, G., I. Honkonen, T. Živković, L. Palin, E. Kallio, K. Ågren, H. Opgenoorth,
671 E. I. Tanskanen, and S. Milan (2016), One year in the Earth's magnetosphere: A
672 global MHD simulation and spacecraft measurements, *Space Weather*, *14*, 351–
673 367, doi:10.1002/2015SW001355.
- 674 Facskó, G., T. B. Balogh, E. I. Anekallu, C. R. and Tanskanen, P. Peitso, L. Degener,
675 M. Kangwa, T. Laitinen, and S. Laakso, H. Burley (in preparation), Bow shock
676 identification in cluster measurements, *Space Weather*.
- 677 Fazakerley, A. N., A. D. Lahiff, R. J. Wilson, I. Rozum, C. Anekallu, M. West, and
678 H. Bacai (2010a), PEACE Data in the Cluster Active Archive, *Astrophysics and
679 Space Science Proceedings*, *11*, 129–144, doi:10.1007/978-90-481-3499-1_8.
- 680 Fazakerley, A. N., A. D. Lahiff, I. Rozum, D. Kataria, H. Bacai, C. Anekallu,
681 M. West, and A. Åsnes (2010b), Cluster-PEACE In-flight Calibration Status,
682 *Astrophysics and Space Science Proceedings*, *11*, 281–299, doi:10.1007/978-90-481-
683 3499-1_19.
- 684 García, K. S., and W. J. Hughes (2007), Finding the Lyon-Fedder-Mobarry mag-
685 netopause: A statistical perspective, *Journal of Geophysical Research (Space
686 Physics)*, *112*(A6), A06229, doi:10.1029/2006JA012039.
- 687 Gordeev, E., G. Facskó, V. Sergeev, I. Honkonen, M. Palmroth, P. Janhunen, and
688 S. Milan (2013), Verification of the GUMICS-4 global MHD code using empirical
689 relationships, *Journal of Geophysical Research (Space Physics)*, *118*, 3138–3146,
690 doi:10.1002/jgra.50359.

- 691 Greenwald, R. A., K. B. Baker, J. R. Dudeney, M. Pinnock, T. B. Jones, E. C.
692 Thomas, J.-P. Villain, J.-C. Cerisier, C. Senior, C. Hanuise, R. D. Hunsucker,
693 G. Sofko, J. Koehler, E. Nielsen, R. Pellinen, A. D. M. Walker, N. Sato,
694 and H. Yamagishi (1995), Darn/Superdarn: A Global View of the Dynam-
695 ics of High-Latitude Convection, *Space Science Reviews*, *71*, 761–796, doi:
696 10.1007/BF00751350.
- 697 Guild, T. B., H. E. Spence, E. L. Kepko, V. Merkin, J. G. Lyon, M. Wiltberger, and
698 C. C. Goodrich (2008a), Geotail and LFM comparisons of plasma sheet clima-
699 tology: 1. Average values, *Journal of Geophysical Research (Space Physics)*, *113*,
700 A04216, doi:10.1029/2007JA012611.
- 701 Guild, T. B., H. E. Spence, E. L. Kepko, V. Merkin, J. G. Lyon, M. Wiltberger, and
702 C. C. Goodrich (2008b), Geotail and LFM comparisons of plasma sheet climatol-
703 ogy: 2. Flow variability, *Journal of Geophysical Research (Space Physics)*, *113*,
704 A04217, doi:10.1029/2007JA012613.
- 705 Gustafsson, G., R. Bostrom, B. Holback, G. Holmgren, A. Lundgren, K. Stasiewicz,
706 L. Ahlen, F. S. Mozer, D. Pankow, P. Harvey, P. Berg, R. Ulrich, A. Pedersen,
707 R. Schmidt, A. Butler, A. W. C. Fransen, D. Klinge, M. Thomsen, C.-G. Faltham-
708 mar, P.-A. Lindqvist, S. Christenson, J. Holtet, B. Lybekk, T. A. Sten, P. Tan-
709 skanen, K. Lappalainen, and J. Wygant (1997), The Electric Field and Wave
710 Experiment for the Cluster Mission, *Space Science Reviews*, *79*, 137–156, doi:
711 10.1023/A:1004975108657.
- 712 Gustafsson, G., M. André, T. Carozzi, A. I. Eriksson, C.-G. Fälthammar, R. Grard,
713 G. Holmgren, J. A. Holtet, N. Ivchenko, T. Karlsson, Y. Khotyaintsev, S. Klimov,
714 H. Laakso, P.-A. Lindqvist, B. Lybekk, G. Marklund, F. Mozer, K. Mursula,
715 A. Pedersen, B. Popielawska, S. Savin, K. Stasiewicz, P. Tanskanen, A. Vaivads,
716 and J.-E. Wahlund (2001), First results of electric field and density observations
717 by Cluster EFW based on initial months of operation, *Annales Geophysicae*, *19*,
718 1219–1240, doi:10.5194/angeo-19-1219-2001.
- 719 Haiducek, J. D., D. T. Welling, N. Y. Ganushkina, S. K. Morley, and D. S. Oz-
720 turk (2017), SWMF Global Magnetosphere Simulations of January 2005: Geo-
721 magnetic Indices and Cross-Polar Cap Potential, *Space Weather*, *15*, 1567–1587,
722 doi:10.1002/2017SW001695.
- 723 Iyemori, T. (1990), Storm-time magnetospheric currents inferred from mid-latitude

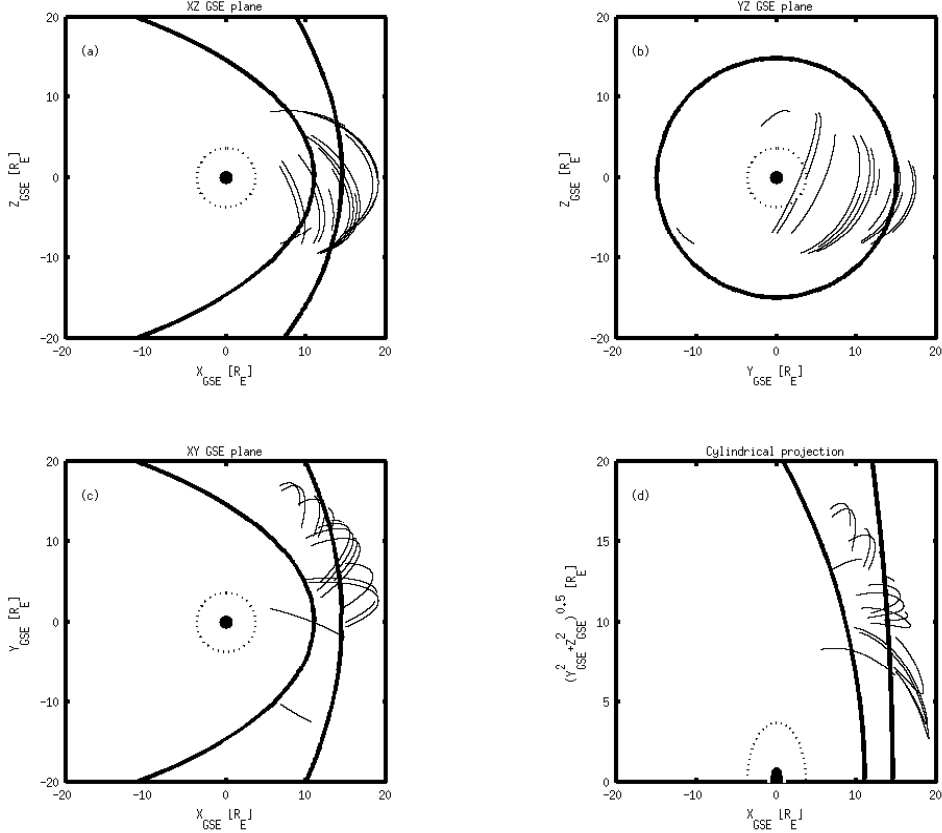
- 724 geomagnetic field variations, *Journal of Geomagnetism and Geoelectricity*, 42,
725 1249–1265, doi:10.5636/jgg.42.1249.
- 726 Janhunen, P., M. Palmroth, T. Laitinen, I. Honkonen, L. Juusola, G. Facskó, and
727 T. I. Pulkkinen (2012), The GUMICS-4 global MHD magnetosphere-ionosphere
728 coupling simulation, *Journal of Atmospheric and Solar-Terrestrial Physics*, 80,
729 48–59, doi:10.1016/j.jastp.2012.03.006.
- 730 Johnstone, A. D., C. Alsop, S. Burge, P. J. Carter, A. J. Coates, A. J. Coker, A. N.
731 Fazakerley, M. Grande, R. A. Gowen, C. Gurgiolo, B. K. Hancock, B. Narheim,
732 A. Preece, P. H. Sheather, J. D. Winningham, and R. D. Woodliffe (1997), Peace:
733 a Plasma Electron and Current Experiment, *Space Science Reviews*, 79, 351–398,
734 doi:10.1023/A:1004938001388.
- 735 Juusola, L., O. Amm, K. Kauristie, and A. Viljanen (2007), A model for estimating
736 the relation between the Hall to Pedersen conductance ratio and ground magnetic
737 data derived from CHAMP satellite statistics, *Annales Geophysicae*, 25, 721–736,
738 doi:10.5194/angeo-25-721-2007.
- 739 Juusola, L., G. Facskó, I. Honkonen, P. Janhunen, H. Vanhamäki, K. Kauristie,
740 T. V. Laitinen, S. E. Milan, M. Palmroth, E. I. Tanskanen, and A. Viljanen
741 (2014), Statistical comparison of seasonal variations in the GUMICS-4 global
742 MHD model ionosphere and measurements, *Space Weather*, 12, 582–600, doi:
743 10.1002/2014SW001082.
- 744 Kallio, E., and G. Facskó (2015), Properties of plasma near the moon in the magne-
745 totail, *Planetary and Space Science*, 115, 69–76, doi:10.1016/j.pss.2014.11.007.
- 746 Kokubun, S., T. Yamamoto, M. H. Acuña, K. Hayashi, K. Shiokawa, and H. Kawano
747 (1994), The GEOTAIL Magnetic Field Experiment., *Journal of Geomagnetism*
748 and *Geoelectricity*, 46, 7–21, doi:10.5636/jgg.46.7.
- 749 Lakka, A., T. I. Pulkkinen, A. P. Dimmock, M. Myllys, I. Honkonen, and M. Palm-
750 roth (2018a), The Cross-Polar Cap Saturation in GUMICS-4 During High Solar
751 Wind Driving, *Journal of Geophysical Research (Space Physics)*, 123, 3320–3332,
752 doi:10.1002/2017JA025054.
- 753 Lakka, A., T. I. Pulkkinen, A. P. Dimmock, E. Kilpua, M. Ala-Lahti, I. Honko-
754 nen, M. Palmroth, and Raukunen (2018b), Icme impact at earth with low and
755 typical mach number plasma characteristics, *Annales Geophysicae Discussions*,
756 <https://doi.org/10.5194/angeo-2018-81>.

- 757 Lani, A., A. Sanna, N. Villedieu, and M. Panesi (2012), COOLFluiD an Open Com-
758 putational Platform for Aerothermodynamics and Flow-Radiation Coupling, in
759 *ESA Special Publication, ESA Special Publication*, vol. 714, p. 45.
- 760 Lyon, J. G., J. A. Fedder, and C. M. Mobarry (2004), The Lyon-Fedder-Mobarry
761 (LFM) global MHD magnetospheric simulation code, *Journal of Atmospheric and*
762 *Solar-Terrestrial Physics*, 66, 1333–1350, doi:10.1016/j.jastp.2004.03.020.
- 763 Mejnertsen, L., J. P. Eastwood, J. P. Chittenden, and A. Masters (2016), Global
764 MHD simulations of Neptune’s magnetosphere, *Journal of Geophysical Research*
765 (*Space Physics*), 121(8), 7497–7513, doi:10.1002/2015JA022272.
- 766 Mejnertsen, L., J. P. Eastwood, H. Hietala, S. J. Schwartz, and J. P. Chittenden
767 (2018), Global MHD Simulations of the Earth’s Bow Shock Shape and Motion
768 Under Variable Solar Wind Conditions, *Journal of Geophysical Research (Space*
769 *Physics*), 123(1), 259–271, doi:10.1002/2017JA024690.
- 770 Mukai, T., S. Machida, Y. Saito, M. Hirahara, T. Terasawa, N. Kaya, T. Obara,
771 M. Ejiri, and A. Nishida (1994), The Low Energy Particle (LEP) Experiment on-
772 board the GEOTAIL Satellite., *Journal of Geomagnetism and Geoelectricity*, 46,
773 669–692, doi:10.5636/jgg.46.669.
- 774 Peredo, M., J. A. Slavin, E. Mazur, and S. A. Curtis (1995), Three-dimensional po-
775 sition and shape of the bow shock and their variation with Alfvénic, sonic and
776 magnetosonic Mach numbers and interplanetary magnetic field orientation, *Jour-*
777 *nal of Geophysical Research*, 100, 7907–7916, doi:10.1029/94JA02545.
- 778 Poedts, S., A. Kochanov, A. Lani, C. Scolini, C. Verbeke, S. Hosteaux, E. Chané,
779 H. Deconinck, N. Mihalache, F. Diet, D. Heynderickx, J. De Keyser, E. De
780 Donder, N. B. Crosby, M. Echim, L. Rodriguez, R. Vansintjan, F. Verstringe,
781 B. Mampaey, R. Horne, S. Glauert, P. Jiggens, R. Keil, A. Glover, G. Deprez, and
782 J.-P. Luntama (2020), The Virtual Space Weather Modelling Centre, *Journal of*
783 *Space Weather and Space Climate*, 10, 14, doi:10.1051/swsc/2020012.
- 784 Powell, K. G., P. L. Roe, T. J. Linde, T. I. Gombosi, and D. L. De Zeeuw (1999), A
785 Solution-Adaptive Upwind Scheme for Ideal Magnetohydrodynamics, *Journal of*
786 *Computational Physics*, 154, 284–309, doi:10.1006/jcph.1999.6299.
- 787 Raeder, J., D. Larson, W. Li, E. L. Kepko, and T. Fuller-Rowell (2008), OpenG-
788 GCM Simulations for the THEMIS Mission, *Space Science Reviews*, 141, 535–555,
789 doi:10.1007/s11214-008-9421-5.

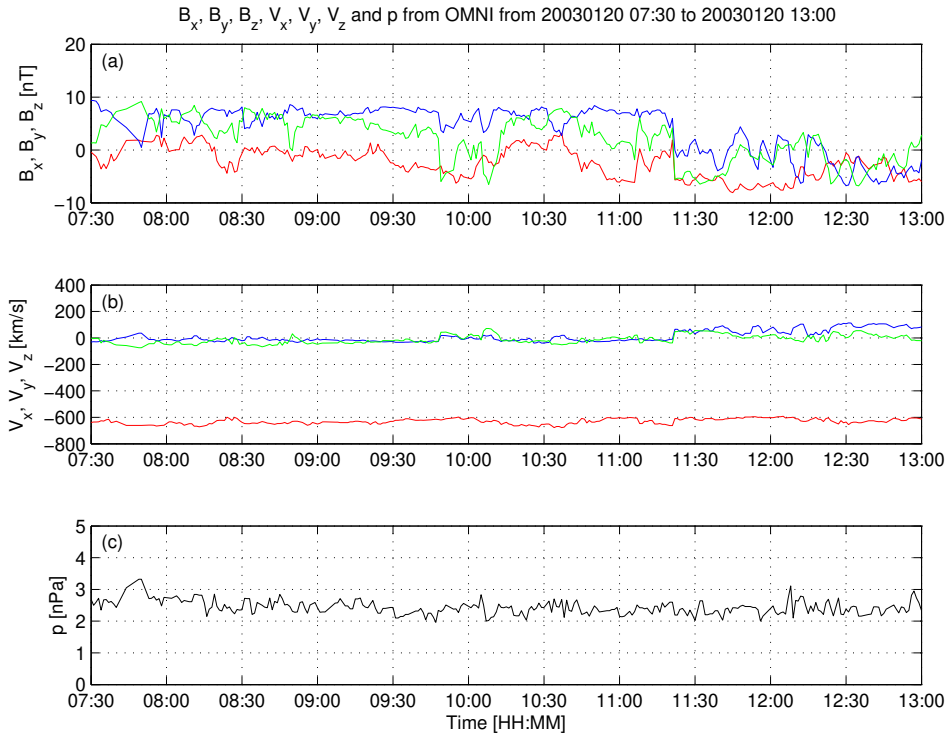
- 790 Reigber, C., H. Lühr, and P. Schwintzer (2002), CHAMP mission status, *Advances*
 791 *in Space Research*, *30*, 129–134, doi:10.1016/S0273-1177(02)00276-4.
- 792 Reme, H., J. M. Bosqued, J. A. Sauvaud, A. Cros, J. Dandouras, C. Aoustin,
 793 J. Bouyssou, T. Camus, J. Cuvilo, C. Martz, J. L. Medale, H. Perrier, D. Rome-
 794 fort, J. Rouzaud, C. D'Uston, E. Möbius, K. Crocker, M. Granoff, L. M. Kistler,
 795 M. Popecki, D. Hovestadt, B. Klecker, G. Paschmann, M. Scholer, C. W. Carl-
 796 son, D. W. Curtis, R. P. Lin, J. P. McFadden, V. Formisano, E. Amata, M. B.
 797 Bavassano-Cattaneo, P. Baldetti, G. Belluci, R. Bruno, G. Chionchio, A. di Lel-
 798 lis, E. G. Shelley, A. G. Ghielmetti, W. Lennartsson, A. Korth, H. Rosenbauer,
 799 R. Lundin, S. Olsen, G. K. Parks, M. McCarthy, and H. Balsiger (1997), The
 800 Cluster Ion Spectrometry (CIS) Experiment, *Space Science Reviews*, *79*, 303–350,
 801 doi:10.1023/A:1004929816409.
- 802 Rème, H., C. Aoustin, J. M. Bosqued, I. Dandouras, B. Lavraud, J. A. Sauvaud,
 803 A. Barthe, J. Bouyssou, T. Camus, O. Coeur-Joly, A. Cros, J. Cuvilo, F. Ducay,
 804 Y. Garbarowitz, J. L. Medale, E. Penou, H. Perrier, D. Romefort, J. Rouzaud,
 805 C. Vallat, D. Alcaydé, C. Jacquay, C. Mazelle, C. D'Uston, E. Möbius, L. M.
 806 Kistler, K. Crocker, M. Granoff, C. Mouikis, M. Popecki, M. Vosbury, B. Klecker,
 807 D. Hovestadt, H. Kucharek, E. Kuenneth, G. Paschmann, M. Scholer, N. Sckopke,
 808 E. Seidenschwang, C. W. Carlson, D. W. Curtis, C. Ingraham, R. P. Lin, J. P.
 809 McFadden, G. K. Parks, T. Phan, V. Formisano, E. Amata, M. B. Bavassano-
 810 Cattaneo, P. Baldetti, R. Bruno, G. Chionchio, A. di Lellis, M. F. Marcucci,
 811 G. Pallocchia, A. Korth, P. W. Daly, B. Graeve, H. Rosenbauer, V. Vasyliunas,
 812 M. McCarthy, M. Wilber, L. Eliasson, R. Lundin, S. Olsen, E. G. Shelley, S. Fuse-
 813 lier, A. G. Ghielmetti, W. Lennartsson, C. P. Escoubet, H. Balsiger, R. Friedel, J.-
 814 B. Cao, R. A. Kovrashkin, I. Papamastorakis, R. Pellat, J. Scudder, and B. Son-
 815 nerup (2001), First multispacecraft ion measurements in and near the Earth's
 816 magnetosphere with the identical Cluster ion spectrometry (CIS) experiment,
 817 *Annales Geophysicae*, *19*, 1303–1354, doi:10.5194/angeo-19-1303-2001.
- 818 Ritter, P., H. Lühr, A. Viljanen, O. Amm, A. Pulkkinen, and I. Sillanpää (2004),
 819 Ionospheric currents estimated simultaneously from CHAMP satellite and IMAGE
 820 ground-based magnetic field measurements: a statistical study at auroral latitudes,
 821 *Annales Geophysicae*, *22*, 417–430, doi:10.5194/angeo-22-417-2004.
- 822 Rostoker, G. (1972), Geomagnetic indices., *Reviews of Geophysics and Space*

- 823 *Physics*, **10**, 935–950, doi:10.1029/RG010i004p00935.
- 824 Siscoe, G. L., G. M. Erickson, B. U. Sonnerup, N. C. Maynard, J. A. Schoendorf,
 825 K. D. Siebert, D. R. Weimer, W. W. White, and G. R. Wilson (2001), The Mag-
 826 netospheric Fluopause, in *AGU Spring Meeting Abstracts*, vol. 2001, pp. SM52D–
 827 02.
- 828 Sofko, G. J., R. Greenwald, and W. Bristow (1995), Direct determination of large-
 829 scale magnetospheric field-aligned currents with SuperDARN, *Geophysical Re-*
 830 *search Letters*, **22**, 2041–2044, doi:10.1029/95GL01317.
- 831 Thomsen, M. F. (2004), Why K_p is such a good measure of magnetospheric convec-
 832 tion, *Space Weather*, **2**, S11004, doi:10.1029/2004SW000089.
- 833 Tóth, G., I. V. Sokolov, T. I. Gombosi, D. R. Chesney, C. R. Clauer, D. L. de
 834 Zeeuw, K. C. Hansen, K. J. Kane, W. B. Manchester, R. C. Oehmke, K. G. Pow-
 835 ell, A. J. Ridley, I. I. Roussev, Q. F. Stout, O. Volberg, R. A. Wolf, S. Sazykin,
 836 A. Chan, B. Yu, and J. Kóta (2005), Space Weather Modeling Framework: A
 837 new tool for the space science community, *Journal of Geophysical Research (Space*
 838 *Physics*), **110**, A12226, doi:10.1029/2005JA011126.
- 839 Tóth, G., B. van der Holst, I. V. Sokolov, D. L. De Zeeuw, T. I. Gombosi, F. Fang,
 840 W. B. Manchester, X. Meng, D. Najib, K. G. Powell, Q. F. Stout, A. Glo-
 841 cer, Y.-J. Ma, and M. Opher (2012), Adaptive numerical algorithms in space
 842 weather modeling, *Journal of Computational Physics*, **231**, 870–903, doi:
 843 10.1016/j.jcp.2011.02.006.
- 844 Trotignon, J. G., P. M. E. Décréau, J. L. Rauch, X. Vallières, A. Rochel,
 845 S. Kouglénou, G. Lointier, G. Facskó, P. Canu, F. Darrouzet, and A. Masson
 846 (2010), The WHISPER Relaxation Sounder and the CLUSTER Active Archive,
 847 *Astrophysics and Space Science Proceedings*, **11**, 185–208, doi:10.1007/978-90-481-
 848 3499-1_12.
- 849 Trotignon, J.-G., Vallières, and the WHISPER team (2011), Calibration report of
 850 the whisper measurements in the cluster active archive (caa), *Tech. rep.*, LPC2E
 851 CNRS, caa-est-cr-whi.
- 852 Tsyganenko, N. A. (1995), Modeling the Earth's magnetospheric magnetic field
 853 confined within a realistic magnetopause, *Journal of Geophysical Research*, **100**,
 854 5599–5612, doi:10.1029/94JA03193.
- 855 Vörös, Z., G. Facskó, M. Khodachenko, I. Honkonen, P. Janhunen, and M. Palmroth

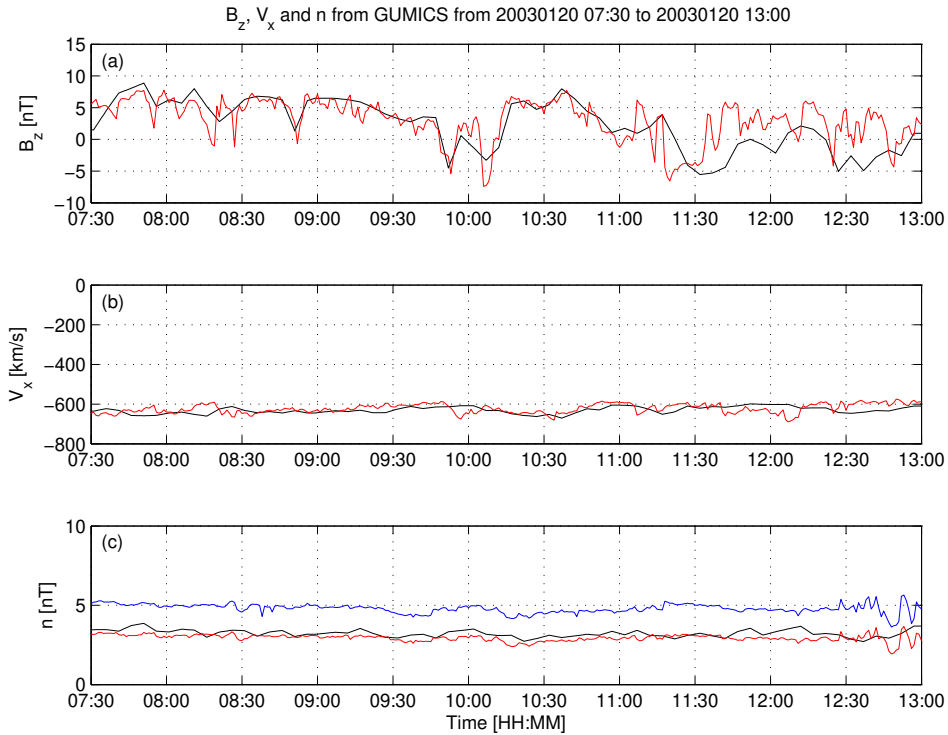
- 856 (2014), Windsock memory COnditioned RAM (CO-RAM) pressure effect: Forced
857 reconnection in the Earth's magnetotail, *Journal of Geophysical Research (Space*
858 *Physics)*, 119, 6273–6293, doi:10.1002/2014JA019857.
- 859 Wang, Z.-D., and R. L. Xu (1994), Signatures of the magnetotail neutral sheet,
860 *Geophysical Research Letters*, 21(19), 2087–2090, doi:10.1029/94GL01960.
- 861 Weimer, D. R. (2005), Improved ionospheric electrodynamic models and applica-
862 tion to calculating Joule heating rates, *Journal of Geophysical Research (Space*
863 *Physics)*, 110, A05306, doi:10.1029/2004JA010884.
- 864 Wiltberger, M., E. J. Rigler, V. Merkin, and J. G. Lyon (2017), Structure of High
865 Latitude Currents in Magnetosphere-Ionosphere Models, *Space Science Reviews*,
866 206, 575–598, doi:10.1007/s11214-016-0271-2.
- 867 Zhang, B., W. Lotko, M. J. Wiltberger, O. J. Brambles, and P. A. Damiano (2011),
868 A statistical study of magnetosphere-ionosphere coupling in the Lyon-Fedder-
869 Mobarry global MHD model, *Journal of Atmospheric and Solar-Terrestrial*
870 *Physics*, 73, 686–702, doi:10.1016/j.jastp.2010.09.027.



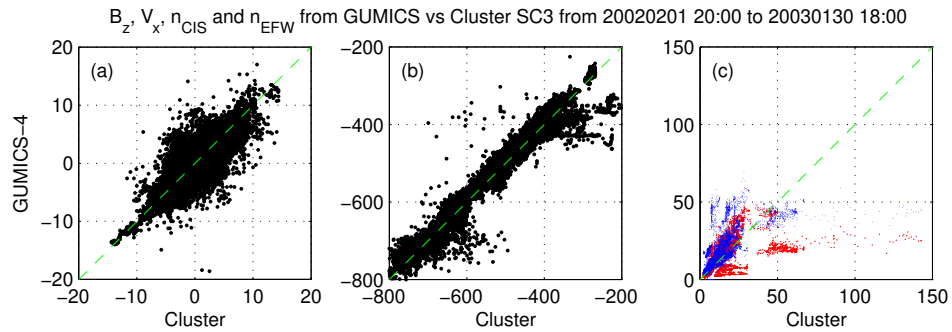
871 **Figure 1.** Cluster SC3 orbit in the solar wind in GSE system for all intervals (see Table 1).
872 (a) XZ (b) YZ (c) XY (d) Cylindrical projection. Average bow-shock and magnetopause posi-
873 tions are drawn on all plots using solid line [Perego *et al.*, 1995; Tsyganenko, 1995, respectively].
874 The black dots at $3.7 R_E$ show the boundary of the GUMICS-4 inner magnetospheric domain.
875 The black circle in the origo of all plots shows the size of the Earth.



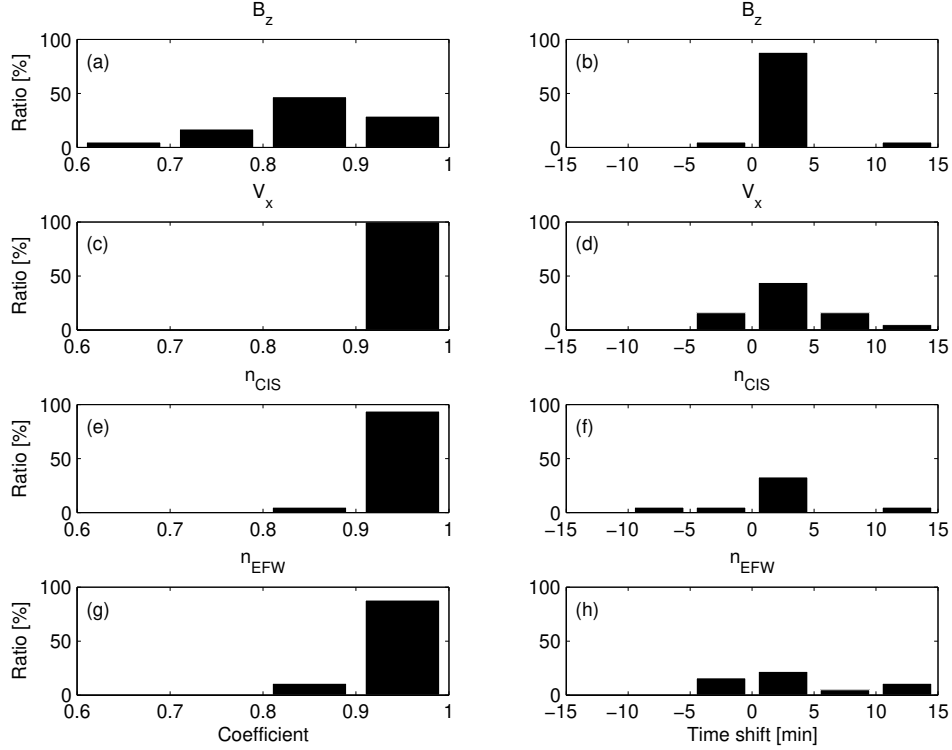
876 **Figure 2.** OMNI solar wind data in GSE system from 7:30 to 13:00 (UT) on January 20,
 877 2003. (a) Magnetic field B_x (red), B_y (green) and B_z (blue) components. (b) Solar wind velocity
 878 V_x (red), V_y (green) and V_z (blue) components. (c) The P pressure of the solar wind (black).



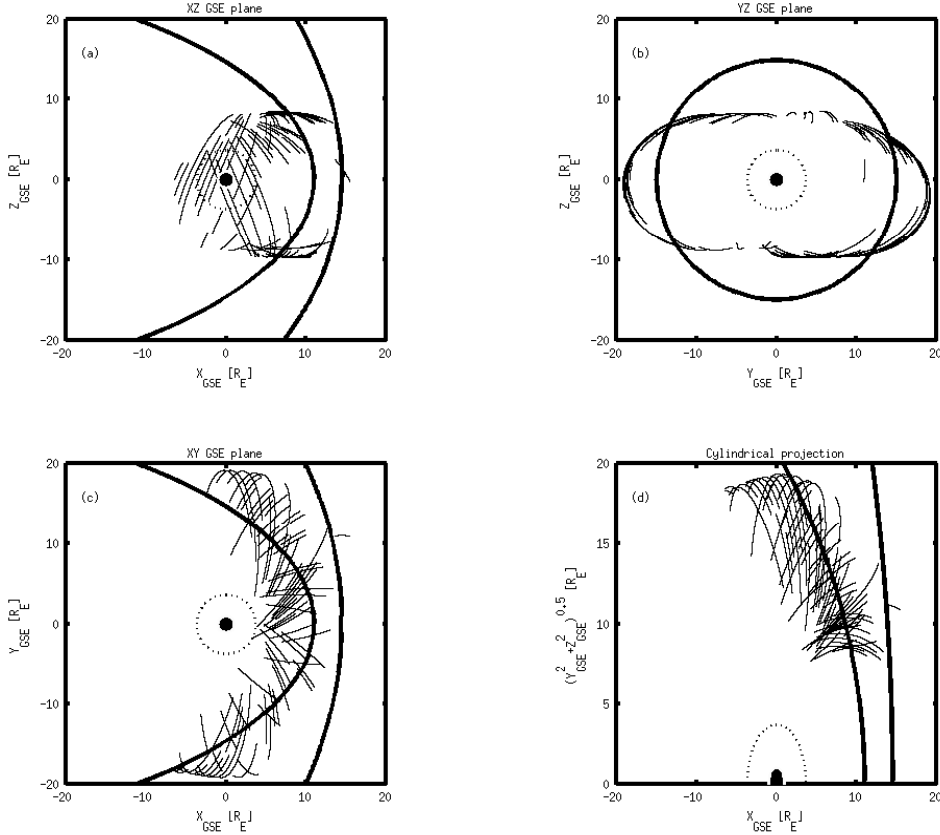
879 **Figure 3.** GUMICS-4 simulation results (black) and Cluster SC3 magnetic field Z component,
 880 ion plasma moments (red) and electron density calculated from spacecraft potential (blue) from
 881 January 20, 2003 from 7:30 to 13:00 (UT) in the solar wind in GSE system. (a) Magnetic field Z
 882 component. (b) Solar wind velocity X component (c) Solar wind density.



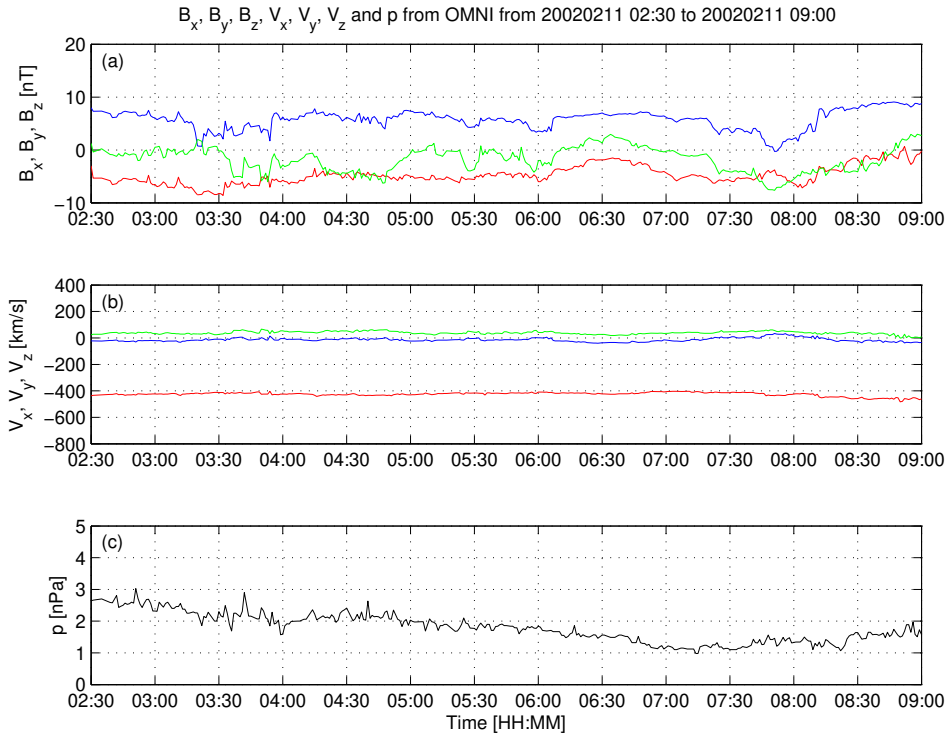
883 **Figure 4.** Scattered plots of the Cluster SC3 and GUMICS-4 simulations for all intervals in
 884 the solar wind. The dashed line is the $y=x$ line. (a) Magnetic field Z component in GSE system.
 885 (b) Solar wind velocity X component in GSE system. (c) Solar wind density measured by the
 886 CIS HIA instrument (red) and calculated from the spacecraft potential (blue).



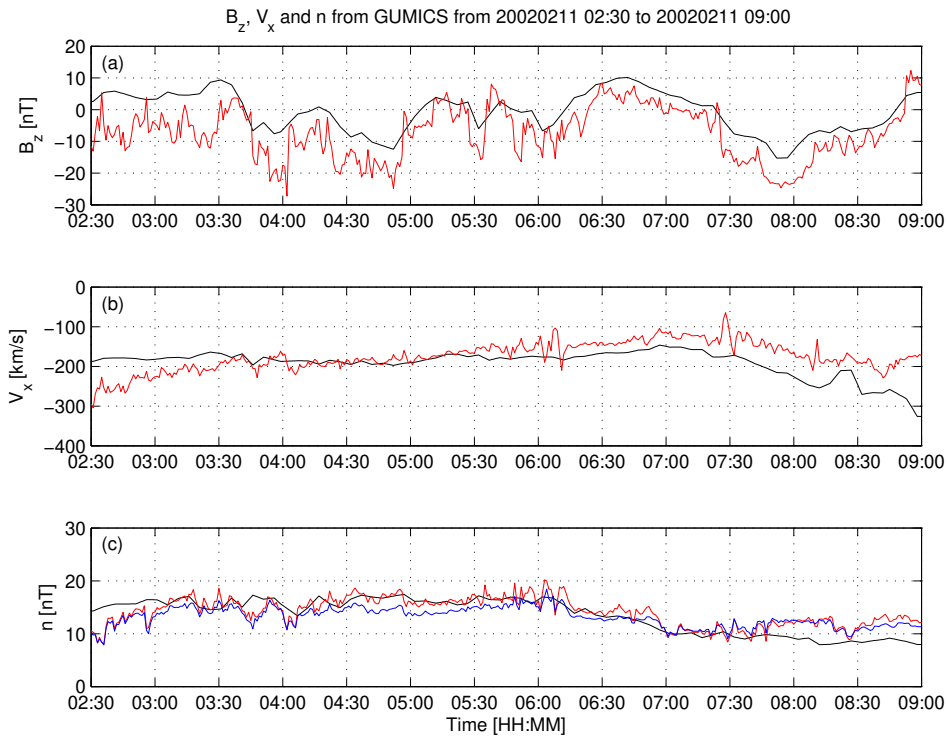
887 **Figure 5.** The distributions of the correlation coefficients (a, c, e, g) of the magnetic field Z
 888 component (B_z) in GSE system, solar wind velocity X component (V_X) in GSE system, the solar
 889 wind density measured by the CIS HIA (n_{CIS}) instrument and calculated from the spacecraft
 890 potential (n_{EFW}), respectively, for all intervals in the solar wind. The distributions of the time
 891 shifts (b, d, f, h) of the B_z , the V_X , the n_{CIS} and the n_{EFW} , respectively, for all intervals in the
 892 solar wind.



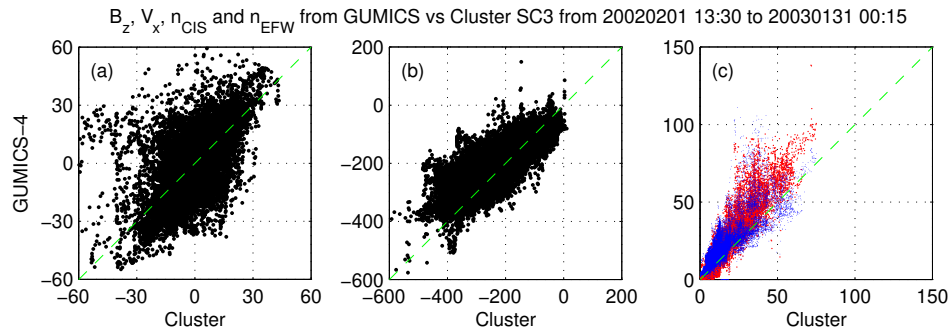
893 **Figure 6.** Cluster SC3 orbit in the magnetosheath in GSE system for all intervals (see Ta-
 894 ble 2). (a) XZ (b) YZ (c) XY (d) Cylindrical projection. Average bow-shock and magnetopause
 895 positions are drawn on all plots using solid line [Peredo *et al.*, 1995; Tsyganenko, 1995, respec-
 896 tively]. The black dots at $3.7 R_E$ show the boundary of the GUMICS-4 inner magnetospheric
 897 domain. The black circle in the origo of all plots shows the size of the Earth.



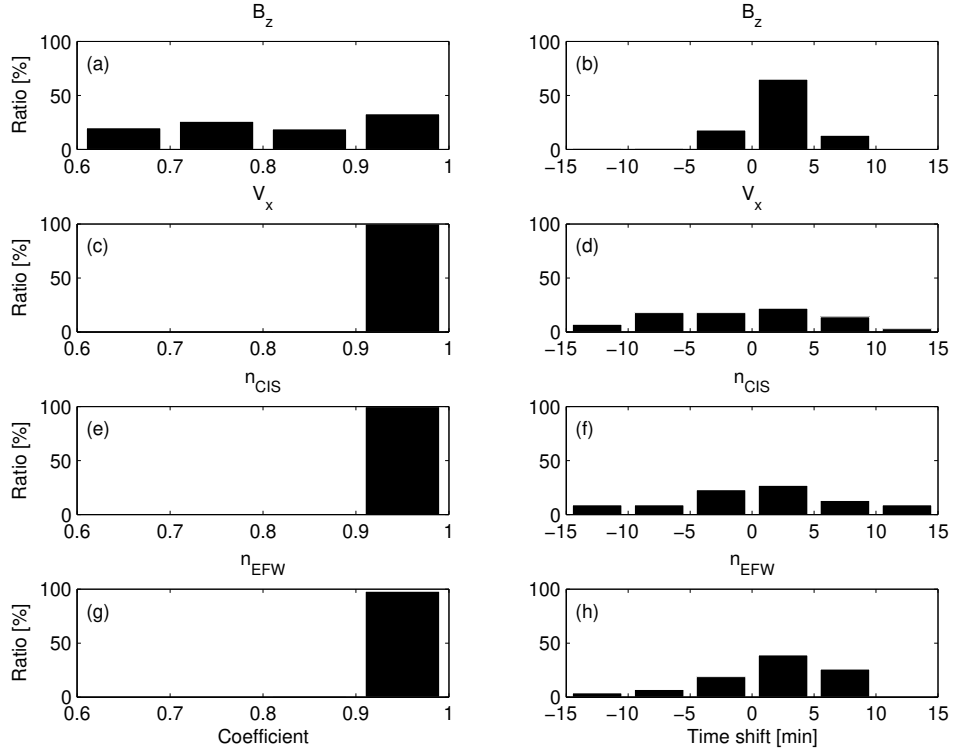
898 **Figure 7.** OMNI solar wind data in GSE system from 2:30 to 09:00 (UT) on February 11,
 899 2002. (a) Magnetic field B_x (red), B_y (green) and B_z (blue) components. (b) Solar wind velocity
 900 V_x (red), V_y (green) and V_z (blue) components. (c) The P pressure of the solar wind (black).



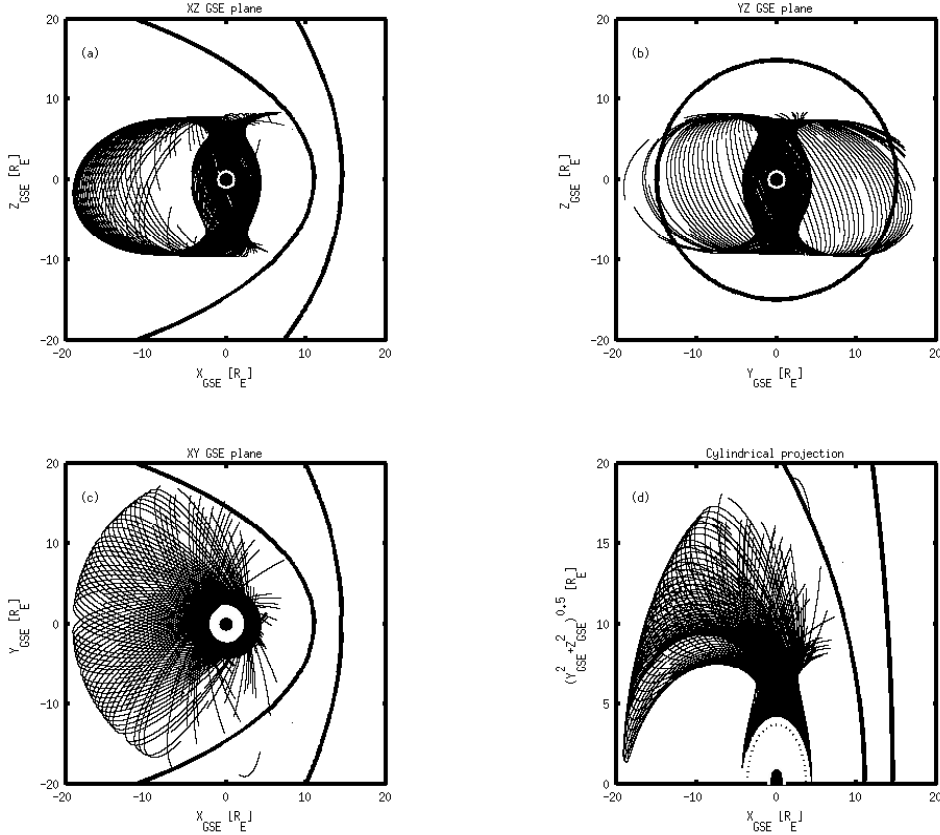
901 **Figure 8.** GUMICS-4 simulation results (black) and Cluster SC3 magnetic field Z component,
902 ion plasma moments (red) and electron density calculated from spacecraft potential (blue) from
903 February 11, 2002 from 2:30 to 9:00 (UT) in the magnetosheath in GSE system (a) Magnetic
904 field Z component. (b) Solar wind velocity X component (c) Solar wind density.



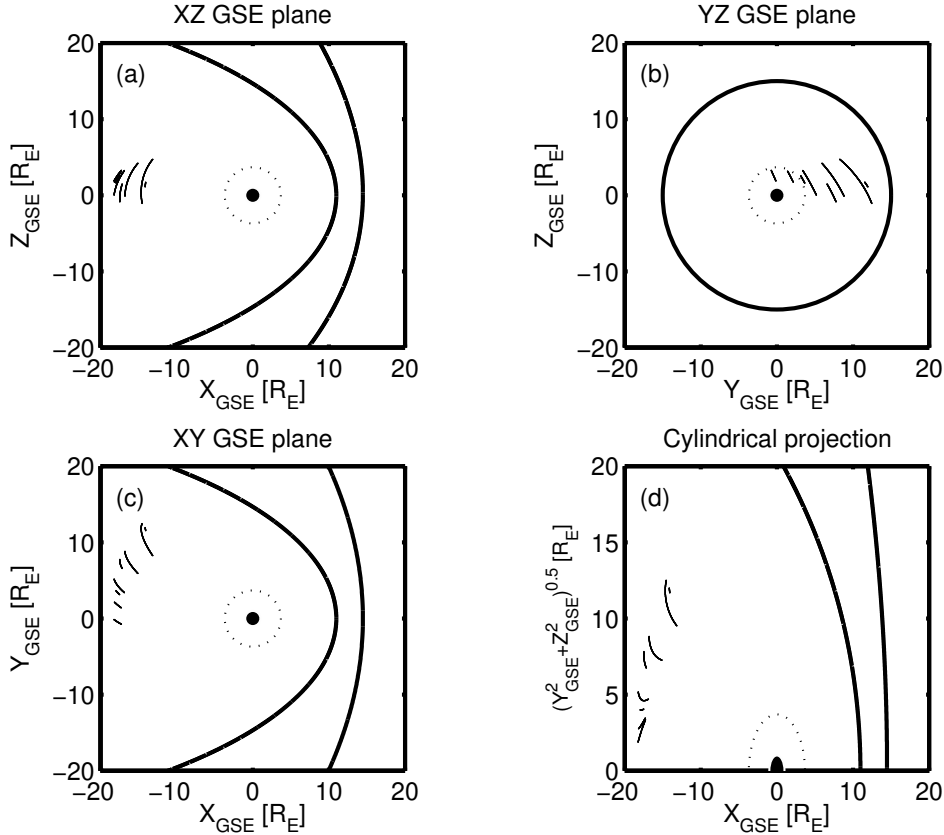
905 **Figure 9.** Scattered plots of the Cluster SC3 and GUMICS-4 simulations for all intervals in
 906 the magnetosheath in GSE system. The dashed line is the $y=x$ line. (a) Magnetic field Z com-
 907 ponent. (b) Solar wind velocity X component. (c) Solar wind density measured by the CIS HIA
 908 instrument (red) and calculated from the spacecraft potential (blue).



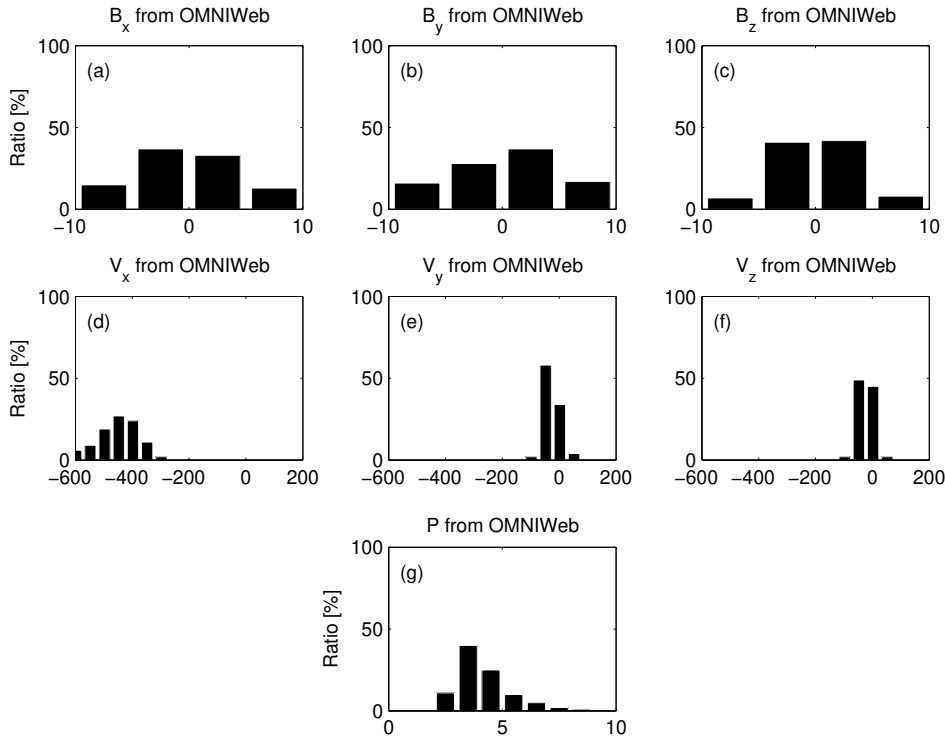
909 **Figure 10.** The distributions of the correlation coefficients (a, c, e, g) of the magnetic field Z
 910 component (B_z) in GSE system, solar wind velocity X component (V_X) in GSE system, the solar
 911 wind density measured by the CIS HIA (n_{CIS}) instrument and calculated from the spacecraft
 912 potential (n_{EFW}), respectively, for all intervals in the magnetosheath. The distributions of the
 913 time shifts (b, d, f, h) of the B_z , the V_X , the n_{CIS} and the n_{EFW}), respectively, for all intervals
 914 in the magnetosheath.



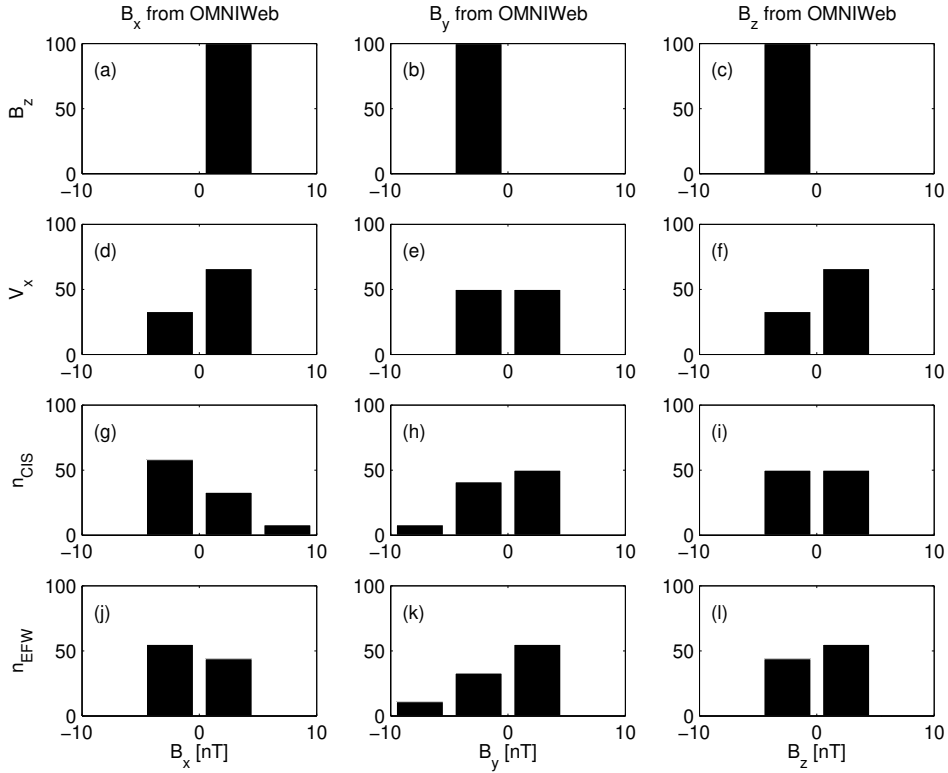
915 **Figure 11.** Cluster SC3 orbit in the magnetosphere in GSE system for all intervals (see Ta-
 916 ble 3). (a) XZ (b) YZ (c) XY (d) Cylindrical projection. Average bow-shock and magnetopause
 917 positions are drawn on all plots using solid line [Peredo *et al.*, 1995; Tsyganenko, 1995, respec-
 918 tively]. The black dots at $3.7 R_E$ show the boundary of the GUMICS-4 inner magnetospheric
 919 domain. The black circle in the origo of all plots shows the size of the Earth.



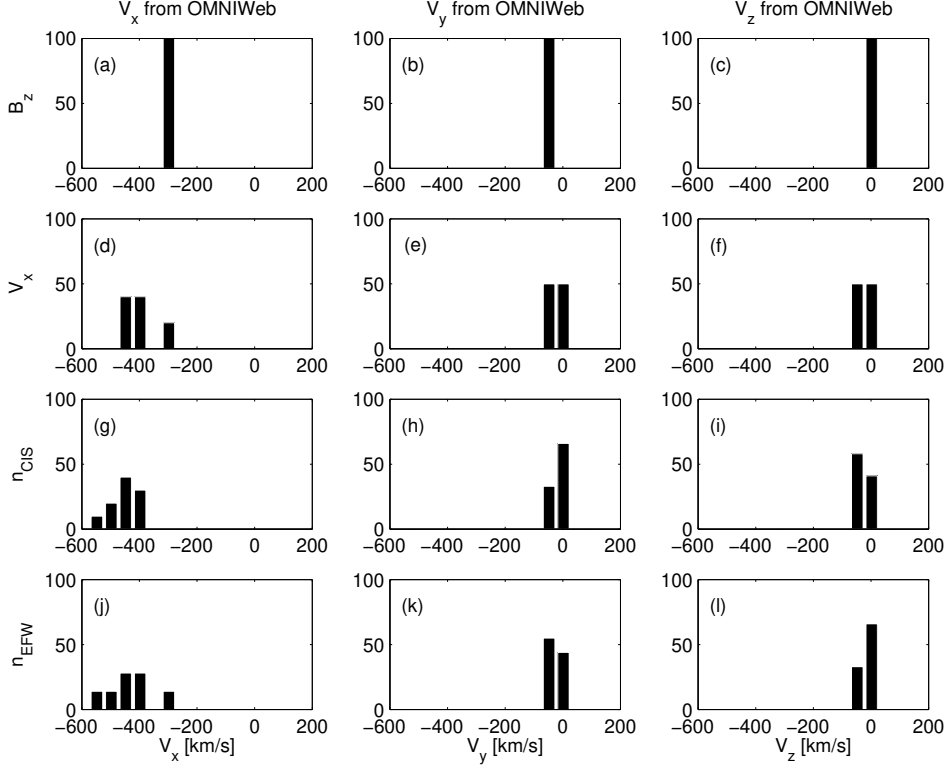
920 **Figure 12.** Cluster SC3 orbit in the tail in GSE system for all intervals (see Table 8). (a)
921 (b) YZ (c) XY (d) Cylindrical projection. Average bow-shock and magnetopause positions
922 are drawn on all plots using solid line [Perego *et al.*, 1995; Tsyganenko, 1995, respectively]. The
923 black dots at $3.7 R_E$ show the boundary of the GUMICS–4 inner magnetospheric domain. The
924 black circle in the origo of all plots shows the size of the Earth.



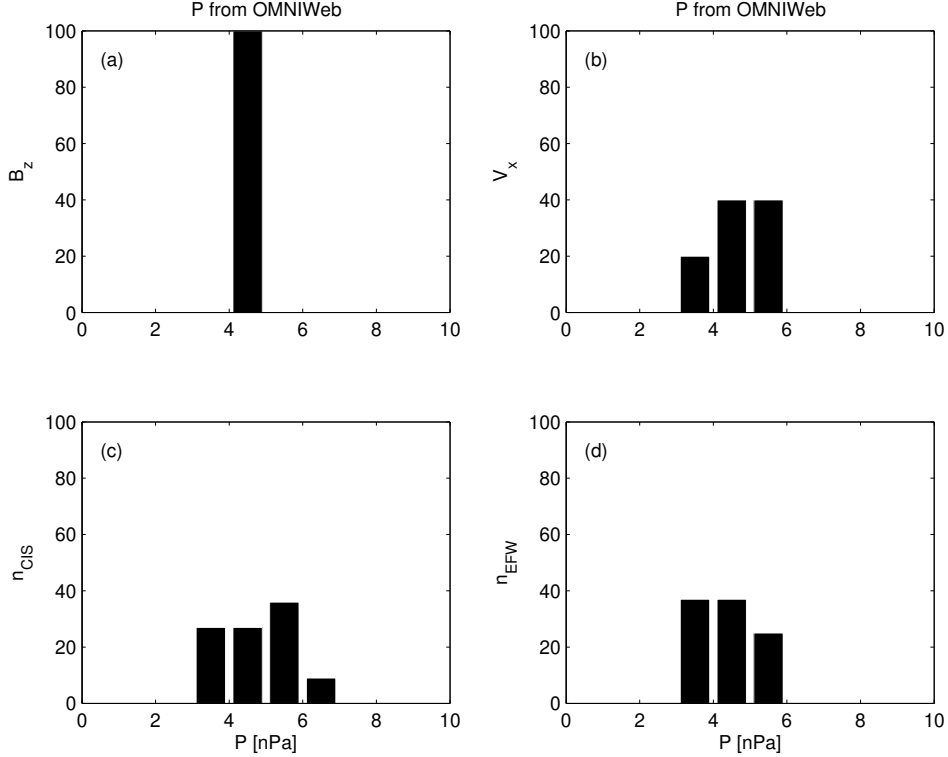
925 **Figure 13.** (a, b, c) The distributions of the OMNI solar wind magnetic field (B_x , B_y , B_z)
 926 components, (d, e, f) the OMNI solar wind velocity (V_x , V_y , V_z) components and (g) the solar
 927 wind dynamic pressure during the 1-year run from January 29, 2002 to February 2, 2003 in GSE
 928 reference frame, respectively. The relative values are given on the vertical axis of all plots in
 929 percentage.



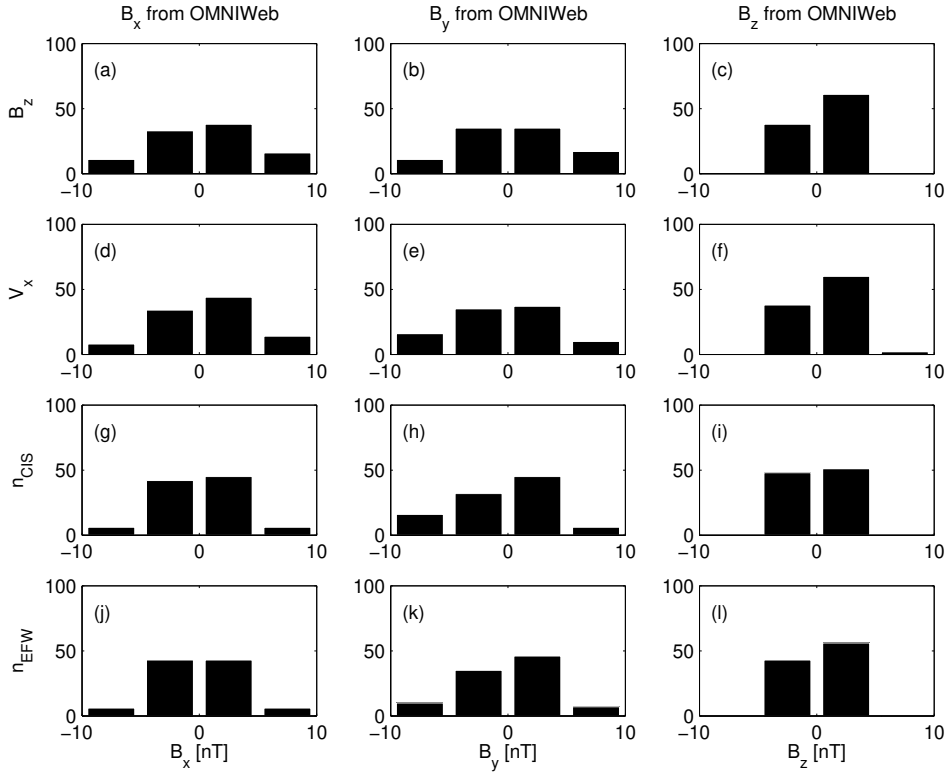
930 **Figure 14.** The distributions of the B_x , the B_y and the B_z OMNI solar wind magnetic field
 931 components when the agreement of the Cluster SC3 measurements and the GUMICS–4 simu-
 932 lations are poor in the solar wind (see Table 4). The B_z , the V_x , the n_{CIS} and the n_{EFW} are
 933 the magnetic field GSE Z component, the plasma ion velocity X GSE component, the solar wind
 934 density measured by the CIS HIA instrument and the calculated from the EFW spacecraft po-
 935 tential, respectively. (a, b, c) Distribution of OMNI B_x , B_y , B_z when the agreement of B_z is
 936 poor. (d, e, f) Distribution of OMNI B_x , B_y , B_z when the agreement of V_x is poor. (g, h, i)
 937 Distribution of OMNI B_x , B_y , B_z when the agreement of n_{CIS} is poor. (j, k, l) Distribution of
 938 OMNI B_x , B_y , B_z when the agreement of n_{EFW} is poor. The values are in percentage unit in
 939 the distributions.



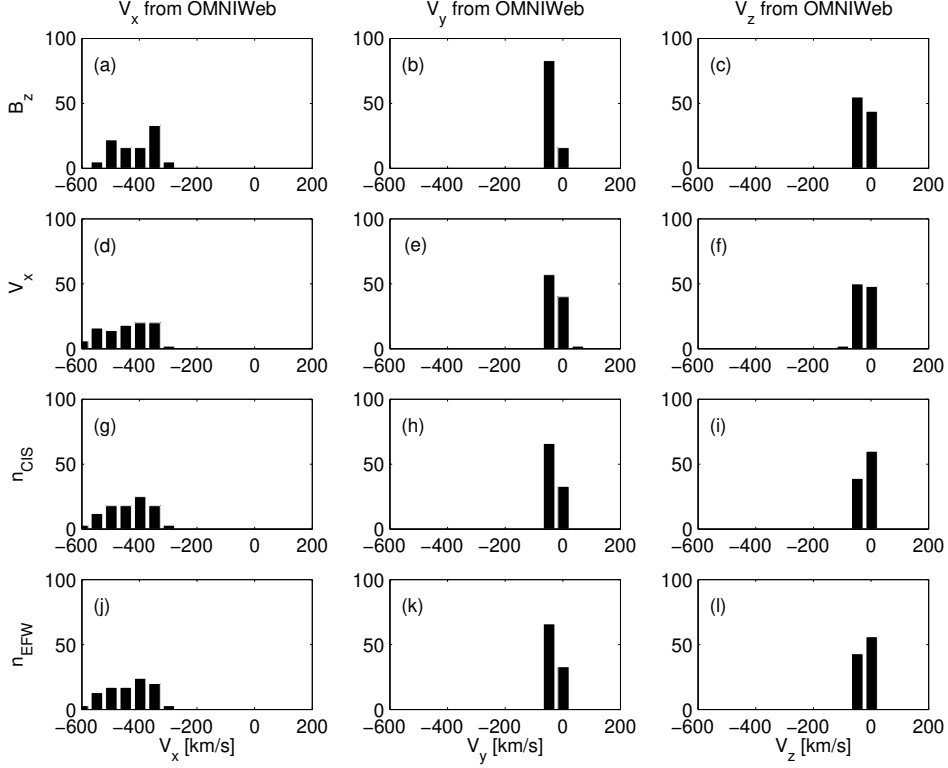
940 **Figure 15.** The distributions of the V_x , the V_y and the V_z OMNI solar wind magnetic field
941 components when the agreement of the Cluster SC3 measurements and the GUMICS–4 simu-
942 lations are poor in the solar wind (see Table 4). The B_z , the V_x , the n_{CIS} and the n_{EFW} are
943 the magnetic field GSE Z component, the plasma ion velocity X GSE component, the solar wind
944 density measured by the CIS HIA instrument and the calculated from the EFW spacecraft po-
945 tential, respectively. (a, b, c) Distribution of OMNI V_x , V_y , V_z when the agreement of B_z is poor.
946 (d, e, f) Distribution of OMNI V_x , V_y , V_z when the agreement of V_x is poor. (g, h, i) Distribution
947 of OMNI V_x , V_y , V_z when the agreement of n_{CIS} is poor. (j, k, l) Distribution of OMNI V_x , V_y ,
948 V_z when the agreement of n_{EFW} is poor. The values are in percentage unit in the distributions.



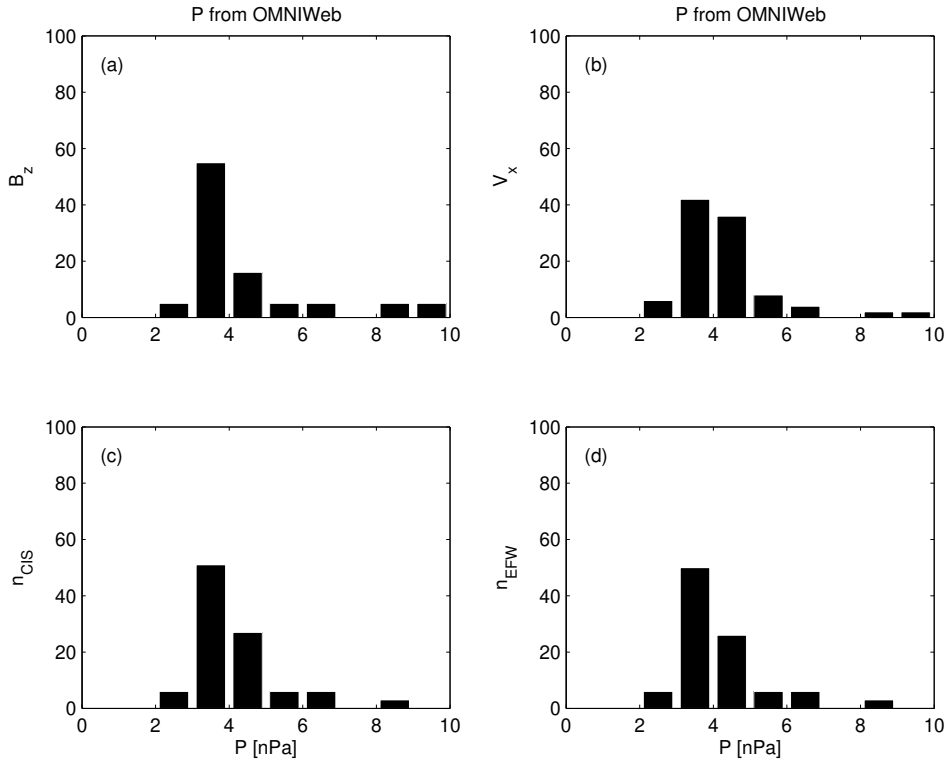
949 **Figure 16.** The distributions of the P solar wind dynamic pressure calculated from OMNI
 950 parameters when the agreement of the Cluster SC3 measurements and the GUMICS–4 simula-
 951 tions are poor in the solar wind (see Table 4). The B_z , V_x , n_{CIS} and n_{EFW} are the magnetic
 952 field GSE Z component, the velocity X GSE component, the solar wind density measured by the
 953 CIS HIA instrument and calculated from the EFW spacecraft potential, respectively. (a, b, c, d)
 954 The distribution of the P calculated from OMNI data when the agreement of the B_z , the V_x , the
 955 n_{CIS} or the n_{EFW} are poor. The values are in percentage unit in the distributions.



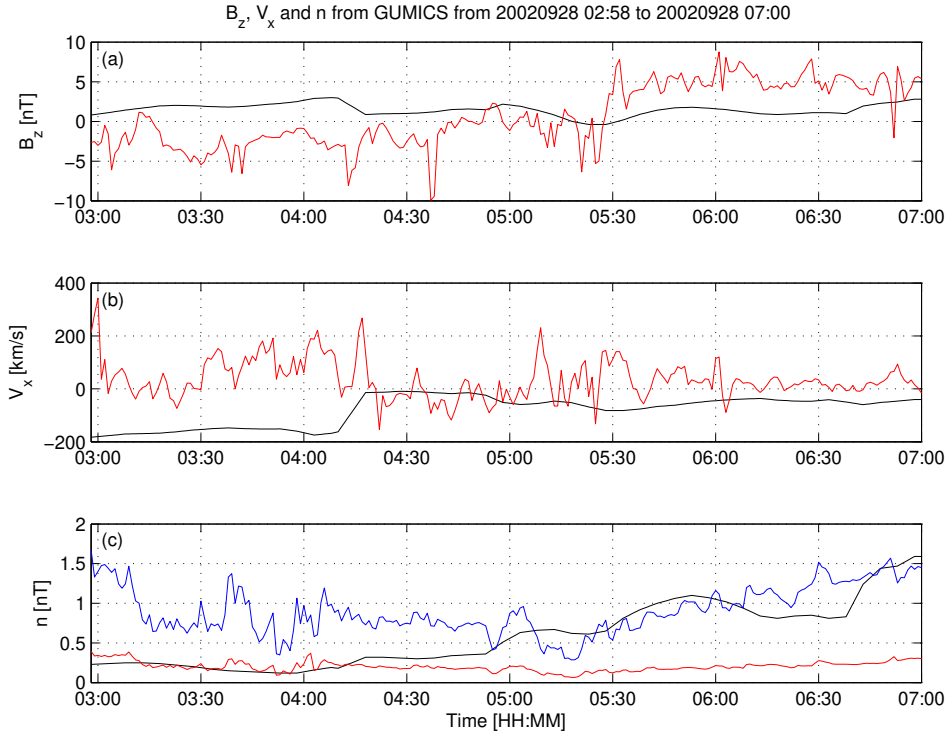
956 **Figure 17.** The distributions of the B_x , the B_y and the B_z OMNI solar wind magnetic field
957 components when the agreement of the Cluster SC3 measurements and the GUMICS–4 simu-
958 lations are poor in the magnetosheath (see Table 5). The B_z , the V_x , the n_{CIS} and the n_{EFW}
959 are the magnetic field GSE Z component, the plasma ion velocity X GSE component, the solar
960 wind density measured by the CIS HIA instrument and the calculated from the EFW spacecraf-
961 t potential, respectively. (a, b, c) Distribution of OMNI B_x , B_y , B_z when the agreement of B_z
962 is poor. (d, e, f) Distribution of OMNI B_x , B_y , B_z when the agreement of V_x is poor. (g, h, i)
963 Distribution of OMNI B_x , B_y , B_z when the agreement of n_{CIS} is poor. (j, k, l) Distribution of
964 OMNI B_x , B_y , B_z when the agreement of n_{EFW} is poor. The values are in percentage unit in
965 the distributions.



966 **Figure 18.** The distributions of the V_x , the V_y and the V_z OMNI solar wind magnetic field
967 components when the agreement of the Cluster SC3 measurements and the GUMICS–4 simula-
968 tions are poor in the magnetosheath (see Table 5). The B_z , the V_x , the n_{CIS} and the n_{EFW} are
969 the magnetic field GSE Z component, the plasma ion velocity X GSE component, the solar wind
970 density measured by the CIS HIA instrument and the calculated from the EFW spacecraft po-
971 tential, respectively. (a, b, c) Distribution of OMNI V_x , V_y , V_z when the agreement of B_z is poor.
972 (d, e, f) Distribution of OMNI V_x , V_y , V_z when the agreement of V_x is poor. (g, h, i) Distribution
973 of OMNI V_x , V_y , V_z when the agreement of n_{CIS} is poor. (j, k, l) Distribution of OMNI V_x , V_y ,
974 V_z when the agreement of n_{EFW} is poor. The values are in percentage unit in the distributions.



975 **Figure 19.** The distributions of the P solar wind dynamic pressure calculated from OMNI pa-
 976 rameters when the agreement of the Cluster SC3 measurements and the GUMICS-4 simulations
 977 are poor in the magnetosheath (see Table 5). The B_z , V_x , n_{CIS} and n_{EFW} are the magnetic
 978 field GSE Z component, the velocity X GSE component, the solar wind density measured by the
 979 CIS HIA instrument and calculated from the EFW spacecraft potential, respectively. (a, b, c, d)
 980 The distribution of the P calculated from OMNI data when the agreement of the B_z , the V_x , the
 981 n_{CIS} or the n_{EFW} are poor. The values are in percentage unit in the distributions.



982 **Figure 20.** GUMICS-4 simulation results (black) and Cluster SC3 magnetic field Z compo-
 983 nent, ion plasma moments (red) and electron density calculated from spacecraft potential (blue)
 984 from September 28, 2002 from 2:58 to 7:00 (UT) in the tail in GSE system. (a) Magnetic field
 985 Z component. (b) Solar wind velocity X component (c) Solar wind density. From 05:15 to 05:30
 986 both the Cluster SC3 and the virtual spaceprobe of the GUMICS-4 simulation cross the neutral
 987 sheet multiple times.

Start/End	C_{B_z}	δt_{B_z}	C_{V_x}	δt_{V_x}	$C_{n_{CIS}}$	$\delta t_{n_{CIS}}$	$C_{n_{EFW}}$	$\delta t_{n_{EFW}}$
	[min]		[min]		[min]		[min]	
20020201 20:00/0203 04:00	0.96	2	1.00	13	0.96	3	0.98	3
20020211 13:00/0212 12:00	0.82	2	1.00	0	0.99	18	0.99	18
20020218 09:00/0219 02:00	0.93	0	1.00	-3	0.94	-3	0.97	-3
20020219 06:30/0219 15:00	0.93	1	1.00	0	0.99	-60	1.00	-52
20020220 18:30/0222 00:00	0.87	4	1.00	4	0.93	-21	0.98	3
20020318 17:30/0319 02:30	0.89	1	1.00	21	0.98	50	0.99	5
20020412 20:30/0413 02:00	0.90	4	0.99	-54	0.94	60	0.98	12
20021227 12:00/1228 03:00	0.75	4	1.00	-3	0.99	-26	0.99	21
20021229 20:00/1230 16:00	0.68	1	1.00	1	0.99	-30	0.98	41
20030106 06:00/0106 19:00	0.79	4	1.00	6	0.99	4	0.99	-60
20030108 07:00/0109 03:30	0.55	10	1.00	41	0.99	10	0.97	-55
20030113 08:30/0113 18:00	0.91	3	1.00	5	1.00	3	0.97	-1
20030120 07:30/0120 13:00	0.82	2	1.00	9	1.00	-6	1.00	-3
20030122 12:00/0123 14:00	0.81	2	1.00	3	0.99	3	0.92	-60
20030124 18:00/0126 00:00	0.73	3	1.00	0	0.99	-60	0.99	60
20030127 16:00/0128 06:00	0.88	-1	1.00	-3	0.95	1	0.88	11
20030129 12:00/0130 18:00	0.90	2	1.00	4	0.94	-59	0.98	1

988 **Table 1.** The studied solar wind intervals. The correlation coefficients (C_{B_z} , C_{V_x} , $C_{n_{CIS}}$,
989 $C_{n_{EFW}}$) and time shift (δt_{V_x} , $\delta t_{n_{CIS}}$, $\delta t_{n_{EFW}}$) in minutes of the magnetic field GSE Z compo-
990 nent (B_z), solar wind velocity X component (V_x), CIS and EFW densities (n_{CIS} , n_{EFW}).

Table 2: The studied magnetosheath intervals. The correlation coefficients (C_{B_z} , C_{V_x} , $C_{n_{CIS}}$, $C_{n_{EFW}}$) and time shift (δt_{V_x} , $\delta t_{n_{CIS}}$, $\delta t_{n_{EFW}}$) in minutes of the magnetic field GSE Z component (B_z), solar wind velocity X component (V_x), CIS and EFW densities (n_{CIS} , n_{EFW}). In the empty slots the correlation calculation gives invalid result.

Start/End	C_{B_z}	δt_{B_z}	C_{V_x}	δt_{V_x}	$C_{n_{CIS}}$	$\delta t_{n_{CIS}}$	$C_{n_{EFW}}$	$\delta t_{n_{EFW}}$
		[min]		[min]		[min]		[min]
20020201 13:30/0201 18:30	0.91	1	0.98	56	0.99	60	0.976	60
20020208 18:15/0209 00:00	0.73	2	0.95	60	0.98	-52	0.98	-54
20020211 02:30/0211 09:00	0.79	0	0.99	-20	0.99	-1	0.99	1
20020212 16:30/0212 21:00	0.80	3	0.99	54	0.99	31	0.99	30
20020219 17:30/0219 23:00	0.76	4	0.98	37	0.99	7	0.99	6
20020222 23:00/0223 06:30	0.64	0	0.97	-60	0.99	-47	0.98	-48
20020227 16:30/0227 23:15	0.48	59	0.98	-31	0.99	-39	1.00	-12
20020310 18:30/0311 00:30	0.97	3	0.98	19	0.99	8	0.99	-2
20020311 14:00/0311 19:00	0.86	5	0.97	36	0.99	-3	0.99	-40
20020406 19:00/0407 01:15	0.76	2	0.96	-60	0.98	-55	0.98	-56
20020410 17:30/0410 23:00	0.89	6	0.99	-50	0.99	3	1.00	5
20020411 11:30/0411 16:30	0.82	4	0.99	39	0.99	3	0.99	3
20020418 18:30/0418 22:45	0.92	60	0.99	-60	0.99	60	0.98	60
20020421 04:30/0421 07:45	0.96	47	0.99	-60	1.00	-60	1.00	-60
20020422 11:45/0422 15:45	0.73	-5	0.98	-17	0.99	-15	0.98	-16
20020423 08:30/0423 12:30	0.93	31	0.99	3	0.99	16	0.99	16
20020430 12:30/0430 17:00	0.79	59	0.98	22	0.98	-18		
20020505 07:00/0505 11:15	0.71	59	0.99	-58	0.98	-60		
20020506 19:15/0507 00:15	0.84	-27	0.98	-60	0.97	-37		
20020507 17:30/0507 23:00	0.93	2	0.98	-30	0.99	-49		
20020514 22:45/0515 03:00	0.79	49	0.99	35	0.99	38	0.99	43
20020517 07:00/0517 12:15	0.74	-5	1.00	-5	0.99	-4	0.99	-3
20020518 13:30/0518 19:30	0.70	1	0.99	9	0.97	-1	0.97	-1

Continued on next page

Table 2 – *Continued from previous page*

Start/End	C_{B_z}	δt_{B_z}	C_{V_x}	δt_{V_x}	$C_{n_{CIS}}$	$\delta t_{n_{CIS}}$	$C_{n_{EFW}}$	$\delta t_{n_{EFW}}$
		[min]		[min]		[min]		[min]
20020519 20:00/0520 03:30	0.98	2	1.00	-9	0.99	-5	0.99	-50
20020520 10:45/0520 20:15	0.77	1	0.99	-3	0.95	-1	0.99	-1
20020522 02:00/0522 08:45	0.49	52	0.99	4	0.99	12	0.99	22
20020527 02:15/0527 17:15	0.79	-3	0.99	-3	0.98	0	0.98	0
20020530 05:00/0530 10:30	0.29	3	1.00	-38	0.99	3	0.99	3
20020601 19:30/0602 01:00	0.68	-2	1.00	18	0.99	-6	0.99	-7
20020602 21:45/0603 17:45	0.62	-5	0.99	-1	0.98	2	0.99	2
20020605 10:30/0606 06:00	0.18	0	1.00	-7	0.97	10	0.98	9
20020607 18:00/0607 22:00	0.92	-35	1.00	-36	0.99	16	0.99	16
20020608 01:15/0608 18:15	0.53	-4	0.99	-39	0.96	-6	0.97	-6
20020610 01:30/0610 09:30	0.76	5	0.99	8	0.99	-5	0.99	-7
20020610 11:00/0611 01:00	0.87	-4	0.99	-33	0.98	23	0.99	6
20020612 18:30/0613 06:15	0.44	-2	0.99	-7	0.97	4	0.97	-32
20020615 07:00/0615 23:30			1.00	47	0.98	-3	0.98	-3
20020617 05:00/0618 03:45	0.76	4	1.00	28	0.98	10	0.98	8
20020620 04:00/0620 11:00	0.61	-8	0.99	-6	0.97	12	0.98	4
20020622 14:30/0622 18:00	0.98	55	1.00	35	0.99	16	1.00	16
20021201 04:15/1202 07:45	0.38	1	1.00	2	0.99	6	0.99	6
20021203 15:30/1204 19:30	0.67	1	0.99	60	0.98	59	0.98	59
20021207 00:30/1207 07:45	0.49	37	0.98	-56	0.99	-19	0.99	-4
20021208 09:30/1209 08:00	0.69	2	0.98	-35	0.97	6	0.98	4
20021212 23:30/1213 14:30	0.51	5	1.00	36	0.99	-3	0.81	-56
20021213 21:15/1214 09:30	0.93	5	0.99	-35	0.99	-13	0.99	-47
20021215 12:45/1216 18:00	0.76	2	0.99	-60	0.94	-60	0.98	31
20021217 16:30/1218 01:45	0.99	2	1.00	-54	0.99	3	0.99	3
20021220 01:30/1220 06:15	0.92	0	1.00	60	0.99	2	0.99	3
20021223 02:15/1223 13:00	0.91	1	0.97	49	0.93	49	0.99	-14
20021223 14:00/1223 22:30	0.84	1	0.99	-2	0.99	-1	1.00	-3
20021224 19:00/1225 01:45	0.94	0	1.00	-44	0.99	26	0.99	27

Continued on next page

Table 2 – *Continued from previous page*

Start/End	C_{B_z}	δt_{B_z}	C_{V_x}	δt_{V_x}	$C_{n_{CIS}}$	$\delta t_{n_{CIS}}$	$C_{n_{EFW}}$	$\delta t_{n_{EFW}}$
		[min]		[min]		[min]		[min]
20021225 23:45/1226 07:15	0.96	7	1.00	-17	0.99	56	0.99	55
20021226 23:00/1227 09:45	0.79	2	1.00	2	0.98	4	0.99	3
20021229 11:45/1229 17:00	0.60	2	1.00	-60	0.98	-19	0.98	50
20021230 17:45/1231 01:00	0.69	1	0.98	52	0.98	60	0.98	22
20021231 23:00/0101 05:15	0.89	2	0.99	15	0.99	-54	1.00	-58
20030105 14:00/0105 21:00	0.69	0	0.99	1	0.98	-60	0.99	-60
20030106 23:15/0107 03:00	0.52	9	0.98	60	0.99	56	1.00	-60
20030109 08:45/0109 16:15			0.91	-56	0.98	-13	0.98	-26
20030110 07:15/0110 15:15	0.94	1	0.99	-7	0.99	1	0.98	5
20030111 08:15/0111 22:30	0.84	0	0.99	-59	0.94	-15	0.94	8
20030112 17:30/0113 00:15	0.98	0	1.00	-52	0.99	39	0.99	51
20030114 00:30/0114 08:30	0.84	-1	0.99	-60	0.98	23	0.98	8
20030116 10:15/0116 17:45	0.62	60	0.93	52	0.99	60	0.99	30
20030117 09:30/0117 13:30	0.68	-3	1.00	8	1.00	-31	0.99	-33
20030118 23:30/0119 03:45	0.93	3	1.00	-12	1.00	7	0.99	7
20030119 21:00/0120 01:00	0.94	3	1.00	5	1.00	38	1.00	19
20030121 06:30/0121 11:30	0.82	-15	0.96	47	0.98	7	0.99	-39
20030122 04:45/0122 09:30	0.69	-2	1.00	10	0.99	-9	0.99	-5
20030126 01:45/0126 06:30	0.85	3	0.99	-15	0.99	-50	0.99	23
20030127 08:15/0127 13:00	1.00	9	1.00	-60	0.98	0	0.99	1
20030128 12:30/0128 17:15	0.77	60	0.99	-24	0.99	-6	0.988	20
20030130 19:45/0131 00:15	0.98	2	0.99	51	0.99	25	0.99	9

Table 3: The studied magnetosphere intervals (UT).

Start/End
20020213 23:00/0214 01:30
20020217 18:30/0218 02:00
20020220 00:45/0220 12:00
20020222 11:15/0222 20:15
20020225 02:15/0225 08:30
20020227 06:00/0227 12:00
20020302 00:00/0302 03:15
20020306 10:00/0306 18:30
20020308 17:30/0309 06:00
20020311 02:15/0311 12:00
20020313 11:15/0314 00:15
20020316 04:45/0316 08:00
20020318 09:00/0318 14:45
20020320 20:30/0320 23:55
20020323 04:00/0323 09:45
20020327 23:45/0328 06:15
20020330 07:15/0330 12:45
20020401 19:30/0401 22:00
20020406 09:30/0406 18:00
20020408 15:00/0409 00:00
20020410 23:30/0411 09:45
20020413 08:30/0413 19:00
20020416 18:00/0417 04:30
20020418 06:00/0418 12:00
20020420 15:00/0420 23:00
20020422 20:00/0423 07:00
20020425 08:30/0425 18:00
20020430 04:40/0430 12:00
20020504 14:30/0504 16:45

Continued on next page

Table 3 – *Continued from previous page*

Start/End
20020505 02:30/0505 07:00
20020507 01:30/0507 15:45
20020508 11:00/0510 04:15
20020512 02:45/0512 09:30
20020514 10:30/0514 12:45
20020519 00:30/0519 19:30
20020521 01:30/0521 22:00
20020523 23:30/0524 02:00
20020524 19:00/0525 08:15
20020526 07:30/0526 10:30
20020528 20:00/0529 05:00
20020531 02:15/0531 13:30
20020602 04:30/0602 07:30
20020602 12:00/0602 21:30
20020604 08:30/0605 07:00
20020606 14:30/0607 16:30
20020609 06:00/0609 20:00
20020611 11:00/0612 13:00
20020614 01:00/0614 16:00
20020616 08:00/0616 18:00
20020620 13:30/0622 01:00
20020623 13:00/0623 17:00
20020624 04:00/0624 10:15
20020630 17:45/0701 15:00
20020701 21:00/0703 10:30
20020703 23:00/0706 03:15
20020707 01:00/0708 23:00
20020710 11:30/0714 03:30
20020714 15:45/0715 15:30
20020716 23:30/0717 16:00

Continued on next page

Table 3 – *Continued from previous page*

Start/End
20020718 05:45/0722 11:00
20020722 23:45/0728 01:00
20020728 02:00/0804 03:45
20020804 04:45/0811 06:15
20020811 07:30/0816 01:00
20020816 15:30/0818 09:00
20020818 10:00/0825 11:30
20020825 13:00/0901 14:15
20020901 17:15/0903 23:30
20020905 02:15/0906 16:30
20020907 10:30/0908 17:00
20020908 18:00/0915 19:30
20020915 21:00/0922 22:30
20020923 00:00/0923 23:30
20020924 03:30/0928 22:45
20020928 23:30/0930 01:00
20020930 02:15/1006 17:00
20021006 17:45/1007 03:30
20021007 05:00/1007 17:30
20021008 07:30/1010 22:00
20021010 22:30/1012 22:30
20021012 23:00/1014 06:30
20021014 09:00/1016 04:00
20021016 14:00/1019 00:15
20021019 01:30/1019 22:00
20021021 04:00/1022 19:30
20021022 22:30/1026 02:30
20021026 04:00/1029 20:15
20021030 01:30/1102 08:00
20021102 22:00/1104 22:00

Continued on next page

Table 3 – *Continued from previous page*

Start/End
20021106 00:00/1107 18:00
20021108 02:00/1109 18:45
20021111 00:00/1112 01:30
20021113 03:45/1114 14:15
20021115 20:30/1116 23:00
20021118 01:00/1118 23:30
20021120 17:00/1121 06:00
20021122 21:30/1124 01:00
20021125 04:00/1126 08:30
20021127 20:00/1128 18:30
20021130 04:00/1201 01:30
20021202 14:30/1203 09:00
20021204 22:00/1205 19:30
20021207 09:00/1207 16:30
20021207 18:00/1207 22:00
20021209 16:30/1210 14:30
20021212 13:45/1212 21:30
20021214 13:30/1214 20:00
20021214 21:00/1215 07:30
20021216 21:00/1217 15:00
20021219 08:00/1219 19:30
20021221 15:45/1221 23:15
20021222 00:30/1222 08:45
20021224 02:30/1224 14:00
20021226 10:00/1226 19:00
20021228 19:30/1229 02:30
20021229 04:00/1229 10:00
20021231 05:00/1231 18:45
20030102 12:30/0102 20:45
20030104 20:45/0105 06:00

Continued on next page

Table 3 – *Continued from previous page*

Start/End
20030105 07:00/0105 13:30
20030107 05:45/0107 21:00
20030109 17:00/0110 00:45
20030112 00:00/0112 09:15
20030112 10:30/0112 16:00
20030114 11:00/0114 20:00
20030116 20:30/0116 22:45
20030119 04:30/0119 09:30
20030119 14:00/0119 17:00
20030121 13:30/0121 21:30
20030126 07:30/0126 15:45
20030128 17:45/0129 08:15
20030131 01:30/0131 11:45

Start/End	OMNI			Cluster SC3			
	B_z [nT]	V_x [km/s]	P [cm $^{-3}$]	B_z	V_x	n_{CIS}	n_{EFW}
20020201 20:00/0203 04:00	-1.25	-373.52	4.08	y	y	n	y
20020211 13:00/0212 12:00	0.03	-533.11	2.18	y	y	y	y
20020218 09:00/0219 02:00	2.56	-362.41	3.46	y	n	n	y
20020219 06:30/0219 15:00	3.55	-401.63	1.25	y	y	n	n
20020220 18:30/0222 00:00	1.95	-440.18	1.96	y	y	n	y
20020318 17:30/0319 02:30	3.79	-429.30	15.34	y	n	n	n
20020412 20:30/0413 02:00	-1.81	-420.35	3.24	y	n	n	y
20021227 12:00/1228 03:00	0.09	-714.40	2.72	y	n	n	y
20021229 20:00/1230 16:00	-0.37	-526.40	2.26	y	y	n	n
20030106 06:00/0106 19:00	2.25	-399.91	1.50	y	n	n	n
20030108 07:00/0109 03:30	-0.58	-280.80	2.97	n	n	y	n
20030113 08:30/0113 18:00	0.68	-397.83	1.72	y	y	y	n
20030120 07:30/0120 13:00	2.16	-630.69	2.43	y	y	y	y
20030122 12:00/0123 14:00	0.13	-608.96	3.41	y	y	y	n
20030124 18:00/0126 00:00	-0.71	-739.68	2.87	y	y	n	n
20030127 16:00/0128 06:00	-0.92	-451.84	3.12	y	y	n	n
20030129 12:00/0130 18:00	-3.09	-450.00	3.96	y	y	n	y

993 **Table 4.** The average OMNI input parameters in the solar wind and the good/bad agreement
994 of the GUMICS–4 simulations to the Cluster B_z magnetic field component, the V_x solar wind
995 speed component, the n_{CIS} solar wind density measured by the Cluster CIS HIA instrument and
996 the n_{EFW} solar wind density calculated from the spacecraft potential measured by the Cluster
997 EFW instrument in the solar wind.

Table 5: The average OMNI input parameters in the solar wind and the good/bad agreement of the GUMICS–4 simulations to the Cluster B_z magnetic field component, the V_x solar wind speed component, the n_{CIS} solar wind density measured by the Cluster CIS HIA instrument and the n_{EFW} solar wind density calculated from the spacecraft potential measured by the Cluster EFW instrument in the magnetosheath.

Start/End	OMNI			Cluster SC3			
	B_z	V_x	P	B_z	V_x	n_{CIS}	n_{EFW}
	[nT]	[km/s]	[cm $^{-3}$]				
20020201 13:30/0201 18:30	0.19	-342.87	4.62	y	n	n	n
20020208 18:15/0209 00:00	-0.48	-508.16	1.61	y	n	n	n
20020211 02:30/0211 09:00	-1.85	-425.67	1.78	y	y	y	y
20020212 16:30/0212 21:00	2.98	-509.22	2.34	y	n	n	n
20020219 17:30/0219 23:00	1.46	-431.50	1.46	y	y	y	y
20020222 23:00/0223 06:30	0.86	-391.22	1.14	y	n	n	n
20020227 16:30/0227 23:15	1.89	-343.13	1.52	n	n	n	n
20020310 18:30/0311 00:30	-2.81	-379.46	1.78	y	y	y	y
20020311 14:00/0311 19:00	1.63	-371.43	2.68	n	n	n	n
20020406 19:00/0407 01:15	-2.71	-333.13	0.93	y	n	n	n
20020410 17:30/0410 23:00	0.31	-312.43	4.42	n	n	y	y
20020411 11:30/0411 16:30	-1.50	-494.02	4.25	y	y	n	n
20020418 18:30/0418 22:45	-0.92	-450.82	0.30	n	n	n	n
20020421 04:30/0421 07:45	0.40	-455.69	1.37	n	n	n	n
20020422 11:45/0422 15:45	0.25	-419.98	1.14	n	n	y	y
20020423 08:30/0423 12:30	2.77	-507.99	6.82	n	n	n	n
20020430 12:30/0430 17:00	2.15	-479.51	3.02	n	n	n	n
20020505 07:00/0505 11:15	0.20	-336.81	1.74	n	n	n	n
20020506 19:15/0507 00:15	0.78	-390.00	2.46	y	n	n	n
20020507 17:30/0507 23:00	2.87	-392.40	3.49	y	n	n	n
20020514 22:45/0515 03:00	-2.42	-414.01	1.82	n	n	n	n

Continued on next page

Table 5 – *Continued from previous page*

Start/End	OMNI			Cluster SC3			
	B_z [nT]	V_x [km/s]	P $[cm^{-3}]$	B_z	V_x	n_{CIS}	n_{EFW}
20020517 07:00/0517 12:15	-0.39	-379.32	1.52	y	y	y	y
20020518 13:30/0518 19:30	0.63	-345.87	1.59	n	n	y	y
20020519 20:00/0520 03:30	4.75	-408.56	1.12	y	y	y	y
20020520 10:45/0520 20:15	0.74	-448.89	1.93	y	y	y	y
20020522 02:00/0522 08:45	-1.07	-398.12	1.63	n	y	y	y
20020527 02:15/0527 17:15	-3.11	-542.53	2.07	y	y	y	y
20020530 05:00/0530 10:30	0.03	-493.86	2.08	y	n	y	y
20020601 19:30/0602 01:00	-3.38	-342.27	4.16	y	y	y	y
20020602 21:45/0603 17:45	0.38	-435.47	1.89	y	y	y	y
20020605 10:30/0606 06:00	-0.42	-394.49	1.08	y	y	n	n
20020607 18:00/0607 22:00	-1.60	-291.85	1.80	y	y	y	y
20020608 01:15/0608 18:15	0.06	-335.39	2.74	y	n	y	y
20020610 01:30/0610 09:30	1.60	-465.52	3.00	y	y	y	y
20020610 11:00/0611 01:00	-2.27	-419.86	2.16	y	n	y	y
20020612 18:30/0613 06:15	-1.13	-351.03	1.16	y	y	y	y
20020615 07:00/0615 23:30	-1.16	-334.27	2.84	n	n	y	y
20020617 05:00/0618 03:45	0.78	-351.47	1.87	y	n	y	y
20020620 04:00/0620 11:00	0.46	-485.48	1.73	y	y	y	y
20020622 14:30/0622 18:00	-0.72	-429.02	1.93	n	n	y	y
20021201 04:15/1202 07:45	-1.09	-499.23	2.62	y	y	y	y
20021203 15:30/1204 19:30	0.34	-449.09	2.06	y	n	n	n
20021207 00:30/1207 07:45	0.80	-451.80	7.33	n	n	y	y
20021208 09:30/1209 08:00	0.60	-600.27	1.49	y	n	y	y
20021212 23:30/1213 14:30	0.10	-337.77	1.32	y	n	n	n
20021213 21:15/1214 09:30	-0.74	-361.19	2.99	y	n	y	y
20021215 12:45/1216 18:00	1.32	-479.48	1.53	y	n	n	n
20021217 16:30/1218 01:45	4.56	-393.99	2.49	y	n	y	y
20021220 01:30/1220 06:15	-1.21	-530.62	3.01	y	n	y	y

Continued on next page

Table 5 – *Continued from previous page*

Start/End	OMNI			Cluster SC3			
	B_z [nT]	V_x [km/s]	P $[cm^{-3}]$	B_z	V_x	n_{CIS}	n_{EFW}
20021223 02:15/1223 13:00	-2.32	-516.12	2.22	y	n	n	n
20021223 14:00/1223 22:30	0.89	-519.77	2.55	y	y	y	y
20021224 19:00/1225 01:45	0.88	-523.86	3.41	y	n	y	y
20021225 23:45/1226 07:15	-0.61	-414.38	2.21	y	y	n	n
20021226 23:00/1227 09:45	-1.79	-618.14	6.20	y	y	y	y
20021229 11:45/1229 17:00	-0.41	-580.12	2.39	y	n	n	n
20021230 17:45/1231 01:00	-1.01	-483.60	1.93	y	n	n	y
20021231 23:00/0101 05:15	0.60	-418.95	1.94	y	n	n	n
20030105 14:00/0105 21:00	-0.03	-414.46	1.69	y	n	n	n
20030106 23:15/0107 03:00	-1.62	-392.29	1.56	n	n	n	n
20030109 08:45/0109 16:15	1.45	-272.82	2.31	n	n	n	n
20030110 07:15/0110 15:15	-2.11	-401.03	2.72	y	n	y	y
20030111 08:15/0111 22:30	-0.20	-433.33	1.24	y	n	n	y
20030112 17:30/0113 00:15	1.53	-389.62	1.45	y	n	n	n
20030114 00:30/0114 08:30	-1.67	-388.53	2.27	y	n	n	y
20030116 10:15/0116 17:45	-1.20	-328.91	1.22	n	n	n	n
20030117 09:30/0117 13:30	-1.36	-327.09	2.55	y	y	y	y
20030118 23:30/0119 03:45	6.41	-459.46	4.82	y	y	y	y
20030119 21:00/0120 01:00	1.52	-597.95	2.38	y	n	y	y
20030121 06:30/0121 11:30	-1.77	-670.25	1.50	y	n	n	n
20030122 04:45/0122 09:30	0.11	-588.87	2.30	y	n	y	y
20030126 01:45/0126 06:30	-0.24	-713.82	2.75	y	y	y	y
20030127 08:15/0127 13:00	7.94	-509.30	0.47	y	n	y	y
20030128 12:30/0128 17:15	4.95	-443.83	4.15	y	y	y	y
20030130 19:45/0131 00:15	4.21	-510.33	2.63	y	n	y	y

Table 6: Intervals around the studied bow shock crossings. The Cluster SC3 crossed the bow shock in all cases. The 2nd column shows whether the bow shock is visible in the GUMICS–4 simulations.

Start/End	GUMICS Bow Shock
20020201 12:00/0202 00:00	+
20020203 00:00/0203 12:00	+
20020206 06:00/0206 18:00	+
20020208 18:00/0209 06:00	+
20020211 06:00/0211 18:00	+
20020212 12:00/0212 18:00	+
20020213 12:00/0213 18:00	+
20020216 00:00/0216 12:00	+
20020217 06:00/0217 12:00	-
20020218 06:00/0218 18:00	+
20020219 00:00/0219 18:00	+
20020220 12:00/0221 00:00	+
20020221 18:00/0222 00:00	+
20020301 06:00/0301 12:00	+
20020304 12:00/0304 18:00	+
20020306 00:00/0306 06:00	+
20020307 00:00/0307 06:00	+
20020308 06:00/0308 12:00	+
20020309 06:00/0309 12:00	+
20020310 12:00/0311 00:00	+
20020311 18:00/0312 00:00	+
20020313 00:00/0313 06:00	-
20020314 00:00/0314 12:00	+
20020316 06:00/0316 18:00	+
20020318 12:00/0319 00:00	+
20020323 12:00/0323 18:00	+

Continued on next page

Table 6 – *Continued from previous page*

Start/End	GUMICS Bow Shock
20020325 18:00/0326 06:00	–
20020327 06:00/0327 12:00	+
20020329 18:00/0330 00:00	–
20020402 00:00/0402 06:00	+
20020405 18:00/0406 00:00	–
20020407 00:00/0407 06:00	–
20020409 06:00/0409 12:00	–
20020410 12:00/0410 18:00	–
20020411 12:00/0411 18:00	–
20020413 00:00/0413 06:00	+
20020413 18:00/0414 06:00	+
20020420 00:00/0420 06:00	+
20020423 12:00/0423 23:00	+
20020427 00:00/0427 06:00	+
20020428 06:00/0428 12:00	+
20020430 18:00/0501 00:00	+
20020505 06:00/0505 18:00	–
20020507 18:00/0509 06:00	+
20020510 06:00/0510 12:00	+
20020513 12:00/0513 18:00	+
20020515 00:00/0515 06:00	–
20020520 00:00/0520 06:00	+
20020522 06:00/0522 12:00	+
20020522 18:00/0523 06:00	+
20021206 06:00/1207 06:00	+
20021218 00:00/1219 00:00	+
20021220 18:00/1221 00:00	+
20021221 00:00/1221 12:00	+
20021222 12:00/1223 00:00	+
20021223 00:00/1223 06:00	+

Continued on next page

Table 6 – *Continued from previous page*

Start/End	GUMICS Bow Shock
20021225 06:00/1226 00:00	+
20021227 06:00/1228 00:00	+
20021228 00:00/1228 12:00	+
20021229 12:00/1230 00:00	+
20030101 06:00/0102 00:00	+
20030103 06:00/0103 12:00	+
20030104 00:00/0104 18:00	+
20030106 00:00/0107 00:00	+
20030108 00:00/0108 12:00	+
20030113 00:00/0114 06:00	+
20030115 00:00/0115 12:00	+
20030118 18:00/0119 00:00	+
20030120 00:00/0121 12:00	+
20030122 06:00/0122 12:00	+
20030123 12:00/0124 00:00	+
20030124 12:00/0124 18:00	+
20030126 00:00/0126 06:00	+
20030127 00:00/0127 18:00	+
20030128 06:00/0128 18:00	+
20030129 06:00/0129 12:00	+
20030130 18:00/0131 00:00	+

Table 7: Intervals around the studied magnetopause crossings.
The Cluster SC3 crossed the magnetopause in all cases. The
2nd column shows whether the magnetopause is visible in the
GUMICS–4 simulations.

Start/End	GUMICS Magnetopause
20020203 06:00/0203 12:00	+
20020206 06:00/0206 12:00	-
20020211 00:00/0211 06:00	+
20020218 00:00/0218 06:00	+
20020225 06:00/0225 12:00	+
20020302 00:00/0302 06:00	+
20020306 18:00/0307 00:00	-
20020308 12:00/0308 18:00	-
20020311 12:00/0311 18:00	+
20020313 18:00/0314 00:00	-
20020314 00:00/0314 06:00	+
20020323 06:00/0323 12:00	+
20020330 12:00/0330 18:00	-
20020404 06:00/0404 12:00	-
20020409 00:00/0409 06:00	-
20020418 12:00/0418 18:00	+
20020422 12:00/0422 18:00	-
20020429 18:00/0430 00:00	-
20020507 12:00/0507 18:00	-
20020509 06:00/0509 12:00	-
20020510 00:00/0510 06:00	-
20020514 18:00/0515 00:00	-
20020519 12:00/0519 18:00	-
20020520 12:00/0521 00:00	-
20020522 00:00/0522 06:00	-
20020529 00:00/0529 12:00	-

Continued on next page

Table 7 – *Continued from previous page*

Start/End	GUMICS Magnetopause
20020530 06:00/0530 18:00	–
20020531 18:00/0601 00:00	–
20020602 18:00/0603 00:00	–
20020604 06:00/0604 12:00	–
20020605 06:00/0606 18:00	–
20020607 12:00/0608 06:00	+
20020609 00:00/0609 06:00	–
20020610 00:00/0610 06:00	–
20020611 00:00/0611 12:00	–
20020612 06:00/0614 00:00	–
20020614 18:00/0615 06:00	–
20020616 00:00/0616 12:00	+
20020620 00:00/0620 18:00	–
20020622 06:00/0622 18:00	–
20020704 12:00/0705 00:00	–
20020706 00:00/0706 12:00	+
20020709 00:00/0709 18:00	–
20020715 18:00/0716 12:00	–
20030105 06:00/0105 18:00	+
20030110 00:00/0110 12:00	+
20030112 12:00/0112 18:00	–
20030117 06:00/0117 12:00	+
20030121 06:00/0121 12:00	+
20030122 00:00/0122 06:00	–
20030126 18:00/0127 00:00	+
20030128 12:00/0128 18:00	+
20030129 00:00/0129 12:00	+
20030131 12:00/0201 00:00	+

Start/End	GUMICS Neutral Sheet
20020901 19:10/0901 23:54	–
20020906 14:07/0906 16:37	+
20020913 17:33/0913 20:06	+
20020918 12:47/0918 14:26	–
20020920 20:36/0921 02:13	+
20020928 02:58/0928 07:00	+
20021002 16:12/1002 23:52	–
20021014 12:34/1014 22:53	+
20021017 03:08/1017 04:11	–

¹⁰⁰¹ **Table 8.** Intervals around the studied neutral sheet crossings in the tail. The Cluster SC3
¹⁰⁰² crossed the neutral sheet in all cases. The 2nd column shows whether the neutral sheet is visible
¹⁰⁰³ in the GUMICS–4 simulations.